

<sup>1</sup> Susceptible host dynamics explain pathogen resilience  
<sup>2</sup>

<sup>3</sup>

<sup>4</sup> Sang Woo Park, . . . , Sarah Cobey

## <sup>5</sup> **Abstract**

<sup>6</sup> Major priority for epidemiological research in the time of anthropogenic change is  
<sup>7</sup> understanding how infectious disease dynamics respond to perturbations. Interven-  
<sup>8</sup> tions to slow the spread of COVID-19 significantly disrupted the transmission of  
<sup>9</sup> other human pathogens, providing unique opportunities to learn about pathogen  
<sup>10</sup> characteristics from spatiotemporal variation in re-emergence patterns. As inter-  
<sup>11</sup> ventions lifted, a key question of whether and when respiratory pathogens would  
<sup>12</sup> eventually return to their pre-pandemic dynamics remains to be answered. To ad-  
<sup>13</sup> dress this gap, we develop a framework for estimating pathogen resilience based on  
<sup>14</sup> how fast epidemic patterns return to their pre-pandemic, endemic dynamics. Our  
<sup>15</sup> analysis reveals a possibility that some pathogens may have settled to endemic cycles  
<sup>16</sup> that are different from their pre-pandemic patterns. Finally, we show that the re-  
<sup>17</sup> plenishment rate of the susceptible pool is a key determinant of pathogen resilience.  
<sup>18</sup> Our framework offers a novel perspective to characterizing the dynamics of endemic  
<sup>19</sup> pathogens and their responses to COVID-19 interventions.

Understanding how ecological systems respond to perturbations is a fundamental challenge in predicting species persistence and extinction [1, 2, 3]. These responses can be characterized in terms of resilience, which often measures how fast a system returns to its stable, reference state following a perturbation [4, 5, 6, 7]. Both theoretical and empirical efforts to quantify resilience of ecological systems have provided key insights for understanding the dynamics of complex systems and linking these findings to actionable strategies for species conservation [8]. However, despite rich literature on ecological resilience, there have been limited applications to measuring the resilience of host-pathogen systems, especially for human pathogens.

Non-pharmaceutical interventions (NPIs) to slow the spread of COVID-19 disrupted the transmission of other human pathogens, providing large-scale natural experiments for understanding how various host-pathogen systems respond to perturbations [9, 10, 11, 12]. In particular, as interventions lifted, large heterogeneities in outbreak dynamics were observed across different pathogens in different countries (Figure 1), likely reflecting differences in NPI patterns, pathogen characteristics, immigration/importation from other countries, and pre-pandemic pathogen dynamics [13]. Even though more than four years have already passed since the emergence of COVID-19, current circulation patterns for many respiratory pathogens appear to be different from their pre-pandemic, seasonal patterns, especially in Hong Kong and Korea: some pathogens, such as human metapneumovirus and bocavirus in Korea, are circulating at lower levels, whereas other pathogens, such as RSV in Korea, seem to exhibit different seasonality (Figure 1). These observations pose two fundamental questions for current and future infectious disease dynamics: (1) can we learn about underlying pathogen characteristics, such as their transmissibility or duration of immunity, from re-emergence patterns? and (2) can we predict whether and when other respiratory pathogens will eventually return to their pre-pandemic dynamics?

To address this question, we propose a framework for characterizing the resilience of a host-pathogen system based on how fast the system recovers from perturbation. We begin by laying out a few representative scenarios that capture the potential impact of COVID-19 interventions on endemic pathogen dynamics and illustrating how resilience can be measured by comparing the pre- and post-pandemic dynamics of susceptible and infected hosts. In practice, information on susceptible hosts are often unavailable, and traditional methods for reconstructing the dynamics of susceptible hosts require long-term endemic time series [14, 15], which cannot be applied due to disruptions in epidemic patterns caused by COVID-19 interventions. Instead, we utilize Takens' embedding theorem to reconstruct empirical attractors from data and further measure the distance from this empirical attractor [16]. This reconstruction allows us to characterize the rate at which this distance decreases over time, which correspond to pathogen resilience. We apply this framework to analyzing pathogen surveillance data for a wide array of respiratory and non-respiratory pathogens from Canada, Hong Kong, Korea, and US. Finally, we show that susceptible host dynamics are a key determinants of pathogen resilience. Our study offers unique insights into understanding pathogen re-emergence patterns following COVID-19 interventions.

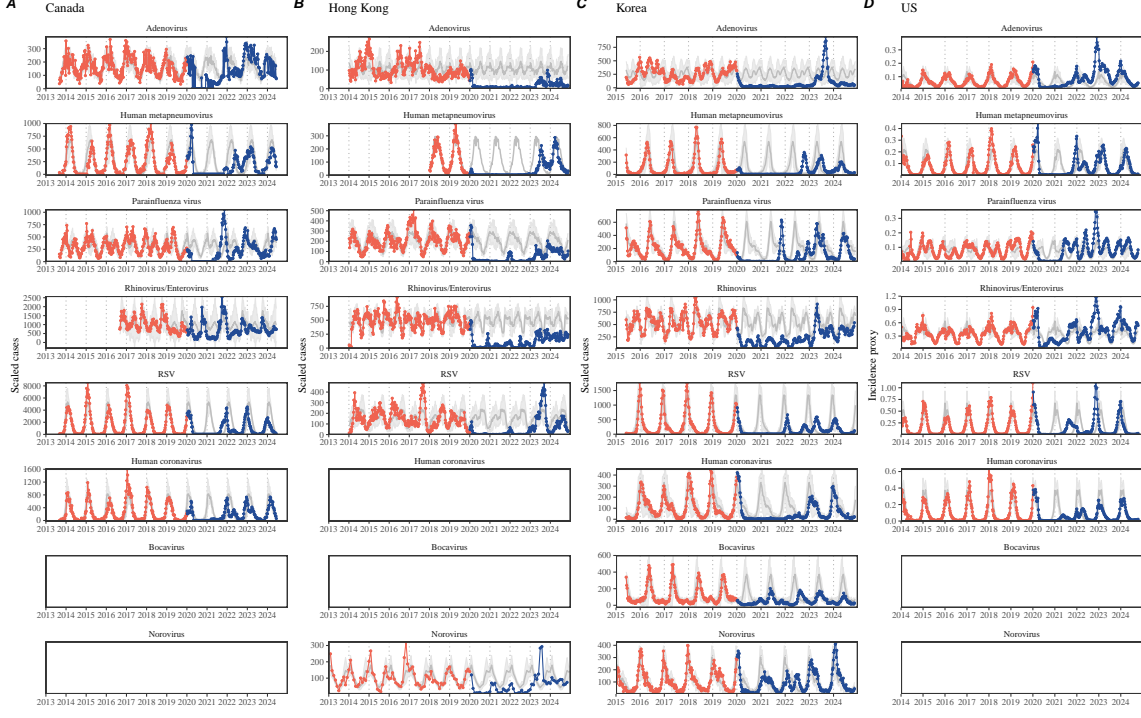


Figure 1: **Observed heterogeneity in responses to COVID-19 pandemic across respiratory pathogens and norovirus in (A) Canada, (B) Hong Kong, (C) Korea, and (D) US.** Red points and lines represent data before 2020. Blue points and lines represent data since 2020. Gray lines and shaded regions represent the mean seasonal patterns and corresponding 95% confidence intervals based on the observed outbreak patterns before 2020.

## 63 Conceptual introduction to pathogen resilience

64 In classical ecological literature, resilience of an ecological system is measured by  
 65 the rate at which the system returns to its reference state following a perturbation  
 66 [4, 5, 6, 7]. This rate corresponds to the largest real part of the eigenvalues of the  
 67 linearized system near equilibrium—here, we refer to this value as the *intrinsic* re-  
 68 silience of the system, which represents the expected rate of return from perturbed  
 69 states. However, respiratory pathogens often exhibit seasonal variation in transmis-  
 70 sion, meaning that the intrinsic resilience of a host-pathogen system varies across  
 71 season. Nonetheless, we can still measure the *empirical* resilience of a host-pathogen  
 72 system by looking at how fast the system returns to the pre-pandemic, endemic  
 73 dynamics after interventions are lifted.

74 As an example, consider an intervention that reduce transmission by 50% for 6  
 75 months starting in 2020, which causes epidemic patterns to deviate from its original  
 76 stable annual cycle for a short period of time and eventually come back (Figure 2A).  
 77 To measure the empirical resilience of this system, we first need to be able to measure

78 the distance from its pre-pandemic attractor. There are many different ways we can  
79 measure the distance from attractor, but for illustrative purposes, we choose one of  
80 the most parsimonious approach: that is, we look at how the susceptible (S) and  
81 infected (I) populations change over time and measure the distance on the SI phase  
82 plane (Figure 2B). In this simple case, the locally estimated scatterplot smoothing  
83 (LOESS) fit indicates that the distance from attractor decreases linearly on average  
84 (Figure 2C). Furthermore, the overall rate of return matches the intrinsic resilience  
85 of the seasonally unforced system (Figure 2C).

86 Alternatively, NPIs can permanently change our behavior and have persisting  
87 impact on the pathogen dynamics; as an example, we consider a scenario in which a  
88 10% reduction in transmission persists even after the NPIs are lifted (Figure 2D–F).  
89 In such cases, we cannot know whether the pathogen will return to its original cycle  
90 or a different cycle until many years have passed after the NPIs are lifted, meaning  
91 that we cannot measure the distance against the new attractor that the system will  
92 eventually approach. Nonetheless, we can still measure the distance against the orig-  
93 inal, pre-pandemic attractor and ask how the distance changes over time (Figure 2E).  
94 The LOESS fit suggests that the distance from the attractor will initially decrease  
95 exponentially on average (equivalently, linearly on a log scale) and eventually plateau  
96 (Figure 2F). Here, a permanent 10% reduction in transmission rate slows down the  
97 system, which causes the distance from the attractor to decrease at a slower rate  
98 (Figure 2F) than it would have otherwise in the absence of permanent transmission  
99 reduction (Figure 2C). This example shows that resilience is not necessarily an in-  
100 trinsic property of a specific pathogen. Instead, pathogen resilience is a property of  
101 a specific attractor that a host-pathogen system approaches, which depends on both  
102 pathogen and host characteristics.

103 Finally, transient phenomena can also complicate the picture (Figure 2G–I). For  
104 example, a stage-structured model for RSV initially exhibits a stable annual cycle,  
105 but perturbations from NPIs cause the epidemic to exhibit biennial cycles (Figure  
106 2G). Despite this biennial cycle, we see that the system eventually approaches the  
107 original pre-pandemic attractor (Figure 2H), suggesting that this biennial cycle is a  
108 transient phenomenon. The LOESS fit indicates that the distance from the attractor  
109 will initially decrease exponentially at a rate that is consistent with the intrinsic  
110 resilience of the seasonally unforced system, but the rate of decrease slows down  
111 as the epidemic exhibits a biennial cycle (Figure 2I). In classical ecological theory,  
112 this behavior is also referred to as a ghost attractor, which causes long transient  
113 dynamics and slow transitions [17]. As we show in Supplementary Figure S1, strong  
114 seasonal forcing in transmission can also lead to transient phenomena for a simple  
115 SIRS model, causing a slowing down of the system.

116 In Supplementary Materials, we also explore measuring the resilience of a two-  
117 strain host-pathogen system: when the dynamics two strains (or two pathogens) are  
118 coupled through cross immunity, we would expect the entire system to be character-  
119 ized by a single resilience value (rather than having two separate resilience for each  
120 strain). Simulations from a simple two-strain system illustrate that separate anal-

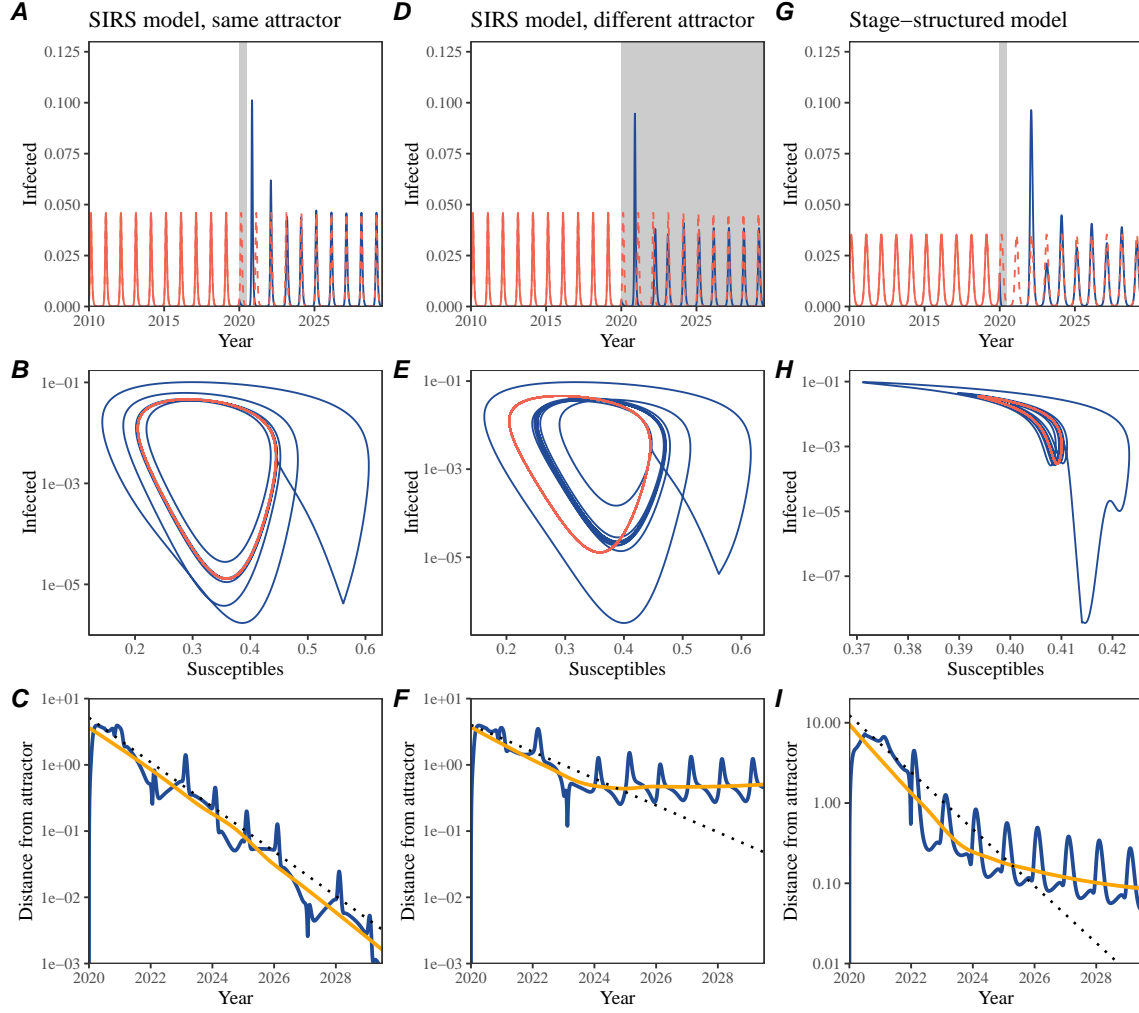


Figure 2: **Conceptual framework for measuring pathogen resilience following NPIs across different scenarios.** (A, D, G) Simulated epidemic trajectories across various models. Red and blue solid lines represent epidemic dynamics before and after interventions are introduced, respectively. Red dashed lines represent counterfactual epidemic dynamics in the absence of interventions. Gray regions indicate the duration of interventions. (B, E, H) Phase plane representation of the corresponding model. Red and blue solid lines represent epidemic trajectories on an SI phase plane before and after interventions are introduced, respectively. (C, F, I) Changes in logged distance from attractor over time. Blue lines represent the logged distance from attractor. Orange lines represent the locally estimated scatterplot smoothing (LOESS) fits to the logged distance from attractor. Dotted lines are superimposed as a comparison to have the same slope as the intrinsic resilience of the seasonally unforced system.

yses of individual strain dynamics (e.g., RSV A vs B) and a joint analysis of total

122 infections (e.g., total RSV infections) yield identical resilience estimates, confirming  
123 our expectation (Supplementary Figure S2, 3). Analogous to a single system, strong  
124 seasonal forcing in transmission can cause the system to slow down through transient  
125 phenomena (Supplementary Figure S4).

126 These observations indicate three possibilities. First, we can directly estimate  
127 the empirical resilience of a host-pathogen system by looking at how fast the system  
128 approaches a pre-pandemic attractor, provided that we can measure the distance  
129 from attractor. The empirical approach to estimating pathogen resilience is partic-  
130 ularly convenient because it does not require us to know the true underlying model.  
131 As we show in Supplementary Figure S5, estimating the intrinsic resilience from fit-  
132 ting standard compartmental models can lead to biased estimates, especially under  
133 model misspecification. Second, resilience estimates allow us to make phenomenolog-  
134 ical predictions about the dynamics of a host-pathogen system following a perturba-  
135 tion: assuming that the distance from the attractor will decrease exponentially over  
136 time, we can obtain a ballpark estimate for when the system will reach an attractor.  
137 Finally, deviation from an exponential decrease in the distance from attractor can  
138 provide information about whether the system has reached an alternative attractor,  
139 or a ghost attractor, that is different from the original, pre-pandemic attractor. These  
140 alternative attractors may reflect continued perturbations from permanent changes  
141 in transmission patterns as well as changes in immune landscapes.

## 142 Inferring pathogen resilience from real data

143 Based on these observations, we now set out to infer pathogen resilience from real  
144 data. Here, we briefly lay out our approach to estimating pathogen resilience from  
145 real data (Figure 3). We then test this approach against simulations and apply it to  
146 real data.

147 So far, we focused on simple examples that assume a constant transmission re-  
148 duction. However, in practice, the impact of NPIs on pathogen transmission is  
149 likely more complex (Figure 3A), reflecting introduction and relaxation of various  
150 intervention strategies. These complexities can lead to longer delays between the  
151 introduction of NPIs and pathogen re-emergence as well as temporal variation in  
152 outbreak sizes (Figure 3B): in this example, continued transmission reduction from  
153 NPIs limits the size of the first outbreak in 2021 following the emergence, allowing  
154 for a larger outbreak in 2022 when NPIs are further relaxed.

155 Previously, we relied on the dynamics of susceptible and infected hosts to compute  
156 the distance from attractor (Figure 2), but information on susceptible hosts are  
157 often not available in practice. In addition, uncertainties in case counts due to  
158 observation error as well as the possibility of complex, multiannual attractor adds  
159 challenges to measuring the distance from attractor. To address these challenges, we  
160 first reconstruct an empirical attractor by utilizing Takens' theorem, which states  
161 that an attractor of a nonlinear multidimensional system can be mapped onto a

162 delayed embedding [16]. Here, we use delayed copies of logged values of pre-pandemic  
 163 cases  $C(t)$  (Figure 3C) to reconstruct the attractor:

$$\langle \log(C(t) + 1), \log(C(t - \tau) + 1), \dots, \log(C(t - (M - 1)\tau) + 1) \rangle, \quad (1)$$

164 where the delay  $\tau$  and embedding dimension  $M$  are determined based on autocor-  
 165 relations and false nearest neighbors, respectively [18, 19]. We then apply the same  
 166 delay and embedding dimensions to the entire time series to determine the position  
 167 on a multi-dimensional state space (Figure 3D), which allows us to measure the  
 168 nearest neighbor distance between the current state of the system and the empirical  
 169 attractor (Figure 3E). In principle, we can quantify how fast this distance decreases  
 170 by fitting a linear regression on a log scale, where the slope of the linear regression  
 171 corresponds to pathogen resilience. As we show in Supplementary Figure S6, over-  
 172 all temporal variations in the distance from attractor, especially the observed rate  
 173 of decrease, appear robust to choices about embedding delays and dimensions; we  
 174 note that using longer delays and higher dimensions tend to smooth out temporal  
 175 variations in the distance from attractor.

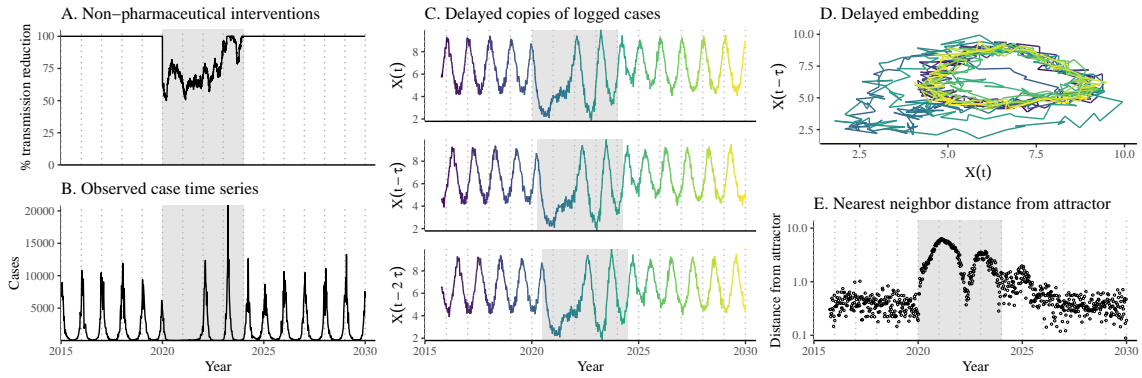


Figure 3: **A schematic diagram explaining how pathogen resilience can be inferred from real data.** (A) A realistic example of a synthetic NPI, represented by a relative reduction in transmission. (B) The impact of the synthetic NPI on epidemic dynamics simulated using a stochastic SIRS model. (C) Generating delayed copies of the logged time series allows us to obtain an embedding. (D) Two dimensional representation of an embedding. (E) Delayed embedding allows us to calculate the nearest neighbor distance from the empirical attractor, which is determined based on the pre-pandemic time series. This distance time series can be used to infer pathogen resilience by fitting a linear regression after choosing an appropriate window for regression.

176 Complex changes in the distance from attractor suggest that estimating pathogen  
 177 resilience from linear regression will likely be sensitive to our choice of fitting windows  
 178 for the regression. In Supplementary Materials, we explore an automated window  
 179 selection criteria for linear regression and test it against randomized, stochastic sim-  
 180 ultations across a wide range of realistic NPI shapes. We find that resilience estimates

181 based on the automated window selection criteria are moderately correlated (0.48)  
182 with the intrinsic resilience of the post-NPI attractor (Supplementary Figure S7). In  
183 contrast, a naive approach that uses the entire time series, starting from the peak  
184 distance, only gives a correlation of 0.09 and consistently underestimates the intrinsic  
185 resilience (Supplementary Figure S7).

186 Now, we apply this approach to pathogen surveillance data presented in Figure  
187 1. For each time series, we apply Takens' theorem independently to reconstruct the  
188 empirical attractor and obtain the corresponding time series of distance from attrac-  
189 tors (Supplementary Figure S8 for the distance time series and linear regression fits).  
190 Then, we use the automated window selection criteria to fit a linear regression and  
191 estimate the empirical resilience for each pathogen in each country. For most res-  
192 piratory pathogens, resilience estimates fall between 0.4/year and 1.8/year (Figure  
193 4A), with the exception of Rhinovirus in the US (0.066/year; 95% CI: 0.018/year–  
194 0.113/year) and Bocavirus in Korea (0.087/year; 95% CI: 0.023/year–0.151/year).  
195 Excluding these exceptions, the mean resilience of common respiratory pathogens is  
196 0.974/year (95% CI: 0.784/year–1.16/year). As a reference, this is  $\approx$  7 times higher  
197 than the intrinsic resilience of pre-vaccination measles dynamics ( $\approx$  0.13/year). Fi-  
198 nally, resilience estimates for norovirus appears to be comparable to the intrinsic  
199 resilience of measles: 0.119/year (95%CI: 0.004/year–0.233/year) for Korea and  
200 0.385/year (95% CI: 0.167/year–0.603/year). A simple ANOVA shows that there  
201 are significant differences in resilience estimates across countries ( $p < 0.036$ ) and  
202 pathogens ( $p < 0.030$ ).

203 Using resilience estimates, we now predict when each pathogen will return to  
204 their original pre-pandemic cycles. Specifically, we extend our linear regression fits  
205 to distance-from-attractor time series and ask when the predicted regression line  
206 will cross a threshold value, which we set to a mean of pre-pandemic distances. We  
207 predict that a return to pre-pandemic cycles would be imminent for most pathogens  
208 (Figure 4B; see Supplementary Figure S9 for a zoomed out version). In addition, we  
209 also predict that many pathogens should have already returned to their pre-pandemic  
210 dynamics by the end of 2024; but these predictions contradict some of the observed  
211 pathogen dynamics. For example, we predict that both human metapneumovirus and  
212 RSV in Korea should have returned to their attractors by now, but the magnitude  
213 and timing of recent epidemics are different from pre-pandemic patterns (Figure 1).  
214 These observations suggest the possibility that some common respiratory pathogens  
215 may have converged to different attractors.

216 In Supplementary Materials, we also consider using a lower threshold for the false  
217 nearest neighbor approach when determining the embedding dimension; this gives  
218 a higher embedding dimension. As explained earlier (Supplementary Figure S6),  
219 this gives a smoother distance-from-attractor time series (compare Supplementary  
220 Figure S10 with S8); this also requires us to use longer time series, which prevents  
221 us from estimating resilience for some pathogens. Overall, resulting estimates of  
222 pathogen resilience with higher embedding dimensions still fall between 0.3/year  
223 and 2.1/year for the most part (Supplementary Figure S11). A direct comparison

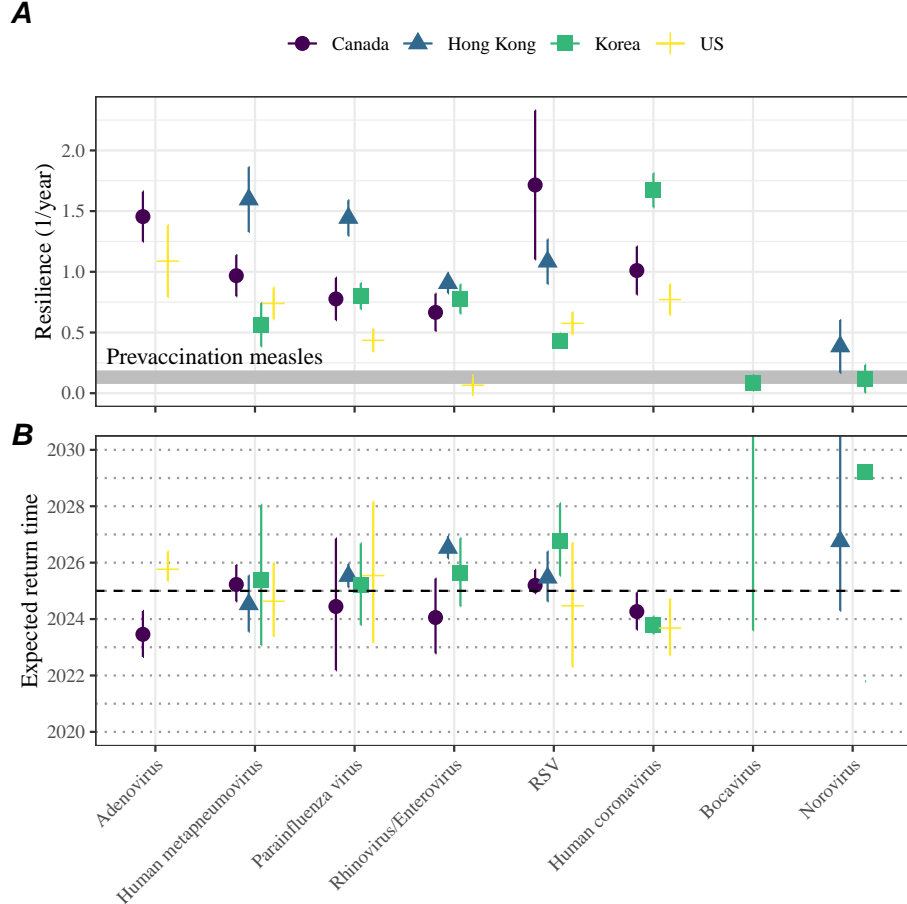


Figure 4: **Summary of resilience estimates.** (A) Estimated pathogen resilience. The gray horizontal line represents the intrinsic resilience of pre-vaccination measles dynamics. (B) Predicted timing of when each pathogen will return to their pre-pandemic cycles. The dashed line in panel B indicates the end of 2024 (current observation time). Error bars represent 95% confidence intervals.

<sup>224</sup> between two approaches (i.e., original estimate vs using higher dimensions) shows a  
<sup>225</sup> strong consistency in resilience estimates (Supplementary Figure S12).

## <sup>226</sup> Susceptible host dynamics explain variation in pathogen <sup>227</sup> resilience

<sup>228</sup> So far, we focused on quantifying pathogen resilience from the observed patterns of  
<sup>229</sup> pathogen re-emergence following COVID-19 interventions. But what factors deter-  
<sup>230</sup> mine how resilient a host-pathogen system is? Here, we use a standard Susceptible-  
<sup>231</sup> Infected-Recovered-Susceptible (SIRS) model to show that susceptible host dynamics

232 are the key determinants of pathogen resilience. To do so, we vary the basic reproduction  
 233 number  $\mathcal{R}_0$ , which represents the average number of secondary infections caused  
 234 by a newly infected individual in a fully susceptible population, and the duration of  
 235 immunity and compute intrinsic resilience for each parameter.

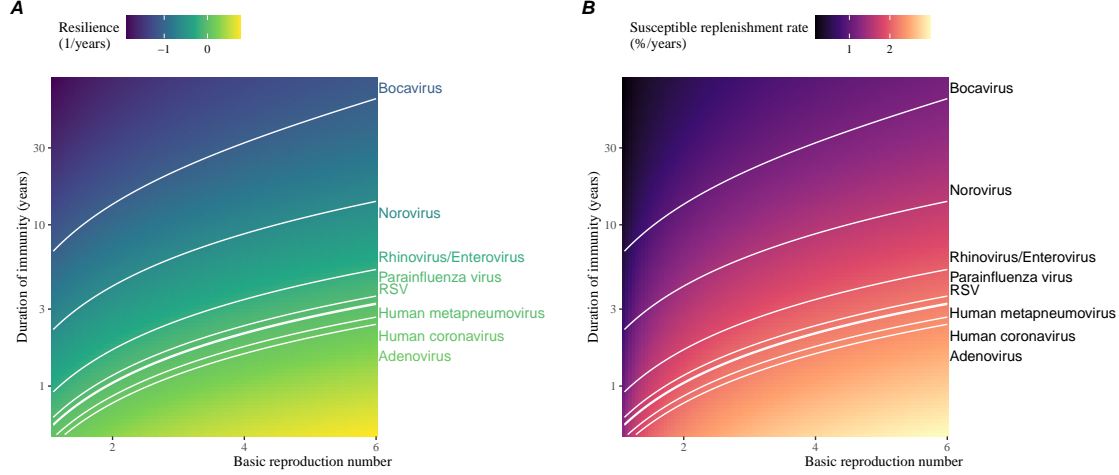


**Figure 5: Linking pathogen resilience to epidemiological parameters and susceptible host dynamics.** (A) The heat map represents intrinsic resilience as a function of the basic reproduction number  $\mathcal{R}_0$  and the duration of immunity. (B) The heat map represents per-capita susceptible replenishment rate as a function of the basic reproduction number  $\mathcal{R}_0$  and the duration of immunity. The standard SIRS model is used to compute intrinsic resilience and per-capita susceptible replenishment rate. Lines correspond to a set of parameters that are consistent with mean resilience estimates for each pathogen. Pathogens are ranked based on their mean resilience estimates, averaged across different countries.

236 We find an increase in  $\mathcal{R}_0$  and a decrease in duration of immunity correspond  
 237 to an increase in pathogen resilience (Figure 5A). These variations can be under-  
 238 stood in terms of the susceptible host dynamics, where faster per-capita susceptible  
 239 replenishment rate causes the system to be more resilient (Figure 5B). This rate can  
 240 be expressed as a ratio between absolute rate at which new susceptibles enter the  
 241 population and the equilibrium number of susceptible individuals in the population,  
 242  $\bar{S}$ . Therefore, both higher  $\mathcal{R}_0$  and shorter duration of immunity can drive faster  
 243 per-capita susceptible replenishment rate (Figure 5B), especially because higher  $\mathcal{R}_0$   
 244 leads to lower  $\bar{S}$ .

245 Finally, we can now rank different pathogens based on the average values of em-  
 246 pirical resilience, which allows us to determine a set of parameters that are consistent  
 247 with the estimated resilience (Figure 5A). Across all pathogens we consider, except  
 248 for bocavirus and norovirus, we estimate that the average duration of immunity is  
 249 likely to be short ( $< 6$  years) across a plausible range of  $\mathcal{R}_0$ . These rankings further

allow us to map each pathogen onto a set of parameters that are consistent with its empirical resilience (Figure 5A) and obtain a plausible range of susceptible replenishment rates for each pathogen (Figure 5B). However, we note that there is no one-to-one correspondence between susceptible replenishment rates and pathogen resilience, leading to a wide uncertainty in the estimates for susceptible replenishment rates (Figure 5B).

## Discussion

The COVID-19 interventions have caused major disruptions to circulation patterns of both respiratory and non-respiratory pathogens, adding challenges to predicting their future dynamics [9, 10, 11, 12]. On the other hand, these interventions offer large-scale natural experiments for understanding how different pathogens respond to perturbations. In this study, we show that pathogen re-emergence patterns following COVID-19 interventions can be characterized through the lens of ecological resilience. Traditionally, ecological resilience measures how fast a system returns to a reference state following a perturbation. In the context of respiratory pathogens, resilience measures how fast epidemics return to their endemic cycles after interventions are lifted.

We use an attractor reconstruction approach to quantify how distance from attractor changes over time for each pathogen [16]. We show that the resilience of a host-pathogen system can be estimated by fitting a linear regression to a logged distance-from-attractor time series. Overall, we estimate that the resilience for most common respiratory pathogens ranges between 0.4/year and 1.8/year, which is 3–14 times more resilient than prevaccination measles, indicating potential challenges in controlling common respiratory pathogens.

Our framework allows us to make phenomenological predictions about when each pathogen will return to their endemic cycles. The ability to predict future epidemic patterns from resilience estimates offers a new paradigm for epidemic forecasting. While this approach cannot predict the exact timing of outbreaks or epidemic patterns, it is nonetheless useful for predicting when epidemics will settle down to regular cycles after a large perturbation, such as COVID-19 interventions.

Our analyses suggest a possibility that several pathogens may have converged to different endemic cycles compared to their pre-pandemic epidemic patterns. Key examples include human metapnuemovirus, RSV, and bocavirus in Korea as well as RSV in Hong Kong. These changes may reflect changes in surveillance or actual shift in the dynamics, caused by permanent changes in behavior or population-level immunity. While it seems unlikely that permanent changes in behavior would only affect a few pathogens and not others, we cannot rule out this possibility given heterogeneity in the age of infection across different respiratory pathogens [SWP: CITE]. A shift in population-level immunity is plausible, as the emergence of SARS-CoV-2 and extinction of influenza B/Yamagata likely caused major changes in immune landscapes;

290 interactions among co-circulating pathogens, such as cross immunity between RSV  
291 and HMPV [20], may have also contributed to changes in population-level immu-  
292 nity. However, we currently do not know how immunity, or lack thereof, from these  
293 pathogens would affect infection from other pathogens. Future studies should use  
294 detailed mechanistic models, coupled with behavioral and immunological data, to  
295 test these hypotheses and better understand post-pandemic dynamics of endemic  
296 pathogens.

297 We show that susceptible host dynamics shape pathogen resilience, where faster  
298 replenishment of the susceptible population causes the pathogen to be more resilient.  
299 For simplicity, we focus on waning immunity and birth as a main driver of the suscep-  
300 tible host dynamics but other mechanisms can also contribute to the replenishment  
301 of the susceptible population. In particular, pathogen evolution, especially the emer-  
302 gence of antigenically novel strains, can cause effective waning of immunity in the  
303 population; therefore, we hypothesize that faster rates of antigenic evolution can also  
304 cause a pathogen to be more resilient. Future studies should explore the relationship  
305 between the rate of evolution and resilience for antigenically evolving pathogens.

306 Quantifying pathogen resilience also offers novel approaches to validating population-  
307 level epidemiological models. So far, the majority of model validation in epidemiology  
308 is based on the ability of a model to reproduce the observed epidemic dynamics and  
309 to predict future dynamics [21, 20, 22, 23, 24]. However, there can be plethora of  
310 models that meet these criteria. For example, two major RSV models have been pro-  
311 posed so far to explain biennial epidemic patterns: (1) a stage- and age-structured  
312 model that allows for disease severity to vary with number of past infections and  
313 age of infection [22] and (2) a pathogen-interaction model that accounts for cross  
314 immunity between RSV and human metapneumovirus [20]. Since both models can  
315 accurately reproduce the observed epidemic patterns, standard criteria for model  
316 validation do not allow us to distinguish between these two models from population-  
317 level data alone. Instead, we can measure the empirical resilience of each model  
318 by simulating various perturbations and compare them to estimates of empirical re-  
319 silience from data, using COVID-19 interventions as an opportunity. Future studies  
320 should further investigate using pathogen resilience for validating epidemic models.

321 There are several limitations to our work. First of all, we did not extensively ex-  
322 plore other approaches to reconstructing the attractor. Recent studies showed that  
323 more sophisticated approaches, such as using non-uniform embedding, can provide  
324 more robust reconstruction for noisy data [19]. In the context of causal inference,  
325 choices about embedding can have major impact on the resulting inference [25]. Our  
326 resilience estimates are likely overly confident given a lack of uncertainties in at-  
327 tractr reconstruction as well as the simplicity of our statistical framework. Short  
328 pre-pandemic time series also contributes to the crudeness of our estimates. Nonethe-  
329 less, as illustrated in our sensitivity analyses (Supplementary Figure S6, S10–S12),  
330 inferences about pathogen resilience appear to be robust to decisions about embed-  
331 ding lags and dimensions—this is because tracking the rate at which the system  
332 approaches the attractor is likely a much simpler problem than making inferences

333 about causal directionality. Our qualitative prediction that common respiratory  
334 pathogens are more resilient than prevaccination measles is also likely to be robust  
335 to these predictions, given how rapid many respiratory pathogens returned to their  
336 original cycles following COVID-19 interventions.

337 Predicting the impact of anthropogenic changes on infectious disease dynamics  
338 is a fundamental aim of infectious disease research in a rapidly changing world.  
339 Our study illustrates that quantifying pathogen resilience can help us understand  
340 how infectious disease pathogens respond to major perturbations caused by public  
341 health interventions. More broadly, a detailed understanding of the determinants of  
342 pathogen resilience may offer unique insights into pathogen persistence and control-  
343 lability.

## 344 Materials and Methods

### 345 Data

346 We gathered time series on respiratory infections from four different countries: Canada,  
347 Hong Kong, Korea, and United States (US). As a reference, we also included time  
348 series data on norovirus infections for available countries—in contrast to respiratory  
349 pathogens, we expect gastrointestinal viruses, such as norovirus, to be less affected  
350 by COVID-19 intervention measures. For all time series, we rounded every year to  
351 52 weeks by taking the average number of cases and tests between the 52nd and  
352 53rd week. We also rescale all time series to account for changes in testing patterns,  
353 which are then used for the actual analysis.

354 Weekly time series of respiratory infection cases in Canada comes from the Res-  
355piratory Virus Detection Surveillance System, which collect data from select lab-  
356oratories across Canada. We extract the data from <https://www.canada.ca/en/public-health/services/surveillance/respiratory-virus-detections-canada.html>. To account for an increase in testing from 2013 to 2024, we calculate a 2 year  
357 moving average for the number of tests for each pathogen, which we use as a proxy  
358 for testing effort. Then, we divide the smoothed testing patterns by the smoothed  
359 value at the final week such that the testing effort has a maximum of 1. We then  
360 divide weekly cases by the testing effort to obtain a scaled case time series. A similar  
361 approach was used earlier for the analysis of RSV time series in the US [22].

362 Weekly time series of respiratory infection cases in Hong Kong comes from the  
363 Centre for Health Protection, Department of Health. We extract the data from  
364 <https://www.chp.gov.hk/en/statistics/data/10/641/642/2274.html>. We also  
365 apply the same scaling procedure to the time series as we did for Canada. For Hong  
366 Kong, we only adjust for testing efforts up to the end of 2019 because there was a  
367 major reduction in testing for common respiratory pathogens since 2020.

368 Weekly time series of acute respiratory infection cases in Korea comes from Ko-  
369 rea Disease Control and Prevention Agency. We extract the data from <https://dportal.kdca.go.kr/pot/is/st/ari.do>. While we do not have information on

373 testing, the reported number of respiratory infections consistently increased from  
 374 2013 to the end of 2019, which we interpreted as changes in testing patterns. Since  
 375 we do not have testing numbers, we used the weekly sum of all acute respiratory vi-  
 376 ral infection cases as a proxy for testing, which were further smoothed with moving  
 377 averaged and scaled to have a maximum of 1. For Korea, we also only adjust for  
 378 testing efforts up to the end of 2019.

379 Finally, weekly time series of respiratory infection cases in the US comes from  
 380 the National Respiratory and Enteric Virus Surveillance System. In the US, there  
 381 has been a large increase in testing against some respiratory pathogens, especially  
 382 RSV, which could not be corrected for through simple scaling. Instead, we derive an  
 383 incidence proxy by multiplying the test positivity with influenza-like illness positivity,  
 384 which is taken from <https://gis.cdc.gov/grasp/fluvview/fluportaldashboard.html>.  
 385 This method of estimatnig an incidence proxy has been recently applied in  
 386 the analysis of seasonal coronaviruses [26] and Mycoplasma pneumoniae infections  
 387 [12]. Detailed assumptions and justifications are provided in [27].

## 388 **Estimating pathogen resilience**

389 In order to measure pathogen resilience from surveillance data, we first reconstruct  
 390 the empirical pre-pandeic attractor of the system using Takens' embedding theorem  
 391 [16]. Specifically, for a given pathogen, we take the pre-pandemic (before 2020)  
 392 case time series  $C(t)$  and reconstruct the attractor using delayed embedding with a  
 393 uniform delay of  $\tau$  and dimension  $M$ :

$$X_{\tau,m}(t) = \langle \log(C(t) + 1), \log(C(t - \tau) + 1), \dots, \log(C(t - (M - 1)\tau) + 1) \rangle. \quad (2)$$

394 Here, the delay  $\tau$  is determined by looking at the autocorrelation of the logged pre-  
 395 pandemic time series and asking when the autocorrelation crosses 0 for the first time  
 396 [19]; a typical delay for for an annual outbreak is around 13 weeks.

397 Then, for a given delay  $\tau$ , we determine the embedding dimension  $M$  using the  
 398 false nearest neighbors approach [18, 19]. To do so, we start with an embedding  
 399 dimension  $e$  and construct a set of points  $A_{\tau,e} = \{X_{\tau,e}(t) | t < 2020\}$ . Then, for each  
 400 point  $X_{\tau,e}(t)$ , we determine the nearest neighbor from the set  $A_{\tau,e}$ , which we denote  
 401  $X_{\tau,e}(t_{nn})$  for  $t \neq t_{nn}$ . Then, if the distance between these two points on  $e+1$  dimension,  
 402  $D_{\tau,e+1}(t) = \|X_{\tau,e+1}(t_{nn}) - X_{\tau,e+1}(t)\|_2$ , is larger than their distance on  $e$  dimension,  
 403  $D_{\tau,e}(t) = \|X_{\tau,e}(t_{nn}) - X_{\tau,e}(t)\|_2$ , these two points are deemed to be false nearest  
 404 neighbors; specifically, we use a threshold  $R$  for the ratio between two distances  
 405  $D_{\tau,e+1}(t)/D_{\tau,e}(t)$  to determine false nearest neighbors. In the main text, we determine  
 406 embedding dimension based as the first dimension without any false nearest neighbors  
 407 for  $R = 10$ . In Supplementary Matereials, we impose  $R = 5$  to select for higher  
 408 dimensions. Once we determine the embedding lag  $\tau$  and dimension  $M$ , we apply  
 409 the embedding to the entire time series and calculate the nearest neighbor distance  
 410 against the attractor  $A_{\tau,M}$  to obtain a time series of distance from attractor  $D_{\tau,M}(t)$ .

411 From a time series of distance from attractor, we estimate pathogen resilience  
 412 by fitting a linear regression to an appropriate window. To automatically select  
 413 the fitting window, we begin by smoothing the distance time series using locally  
 414 estimated scatterplot smoothing (LOESS) to obtain  $\hat{D}_{\tau,M}(t)$ , where the smoothing  
 415 is performed on a log scale and exponentiated afterwards. Then, we determine  
 416 threshold values ( $T_{\text{start}}$  and  $T_{\text{end}}$ ) for the smoothed distances and choose the fitting  
 417 window based on when  $\hat{D}_{\tau,M}(t)$  crosses these threshold values for the first time.  
 418 These thresholds are determined by first calculating maximum distance,

$$\max \hat{D} = \max \hat{D}_{\tau,M}(t), \quad (3)$$

419 and mean pre-pandemic distance,

$$\hat{D}_{\text{mean}} = \frac{1}{N_{t < 2020}} \sum_{t < 2020} \hat{D}_{\tau,M}(t), \quad (4)$$

420 as a reference, and then dividing their ratios into 10 equal bins:

$$T_{\text{start}} = \hat{D}_{\text{mean}} \times \left( \frac{\max \hat{D}}{\hat{D}_{\text{mean}}} \right)^{9/10} \quad (5)$$

$$T_{\text{end}} = \hat{D}_{\text{mean}} \times \left( \frac{\max \hat{D}}{\hat{D}_{\text{mean}}} \right)^{1/10} \quad (6)$$

421 This allows us to discard the initial period during which the distance increases (from  
 422 the introduction of intervention measures) and the final period during which the  
 423 distance plateaus (as the system reaches an attractor). The fitting window is deter-  
 424 mined based on when the smoothed distance  $\hat{D}_{\tau,M}(t)$  crosses these threshold values  
 425 for the first time; then, we fit a linear regression to logged (unsmoothed) distances  
 426  $\log D_{\tau,M}(t)$  using that window.

## 427 Mathematical modeling

428 Throughout the paper, we use a series of mathematical models to illustrate the con-  
 429 cept of pathogen resilience and to understand the determinants of pathogen resilience.  
 430 In general, the intrinsic resilience for a given system is given by the largest real part  
 431 of the eigenvalues of the linearized system at endemic equilibrium. Here, we focus on  
 432 the SIRS model and present the details of other models in Supplementary Materials.  
 433 The SIRS (Susceptible-Infected-Recovered-Susceptible) model is the simplest model  
 434 that allows for waning of immunity, where recovered (immune) individuals are as-  
 435 sumed to become fully susceptible after an average of  $1/\delta$  time period. The dynamics  
 436 of the SIRS model is described by the following set of differential equations:

$$\frac{dS}{dt} = \mu - \beta(t)SI - \mu S + \delta R \quad (7)$$

$$\frac{dI}{dt} = \beta(t)SI - (\gamma + \mu)I \quad (8)$$

$$\frac{dR}{dt} = \gamma I - (\delta + \mu)R \quad (9)$$

(10)

437 where  $\mu$  represents the birth/death rate,  $\beta(t)$  represents the time-varying trans-  
 438 mission rate, and  $\gamma$  represents the recovery rate. The basic reproduction number  
 439  $\mathcal{R}_0 = \beta(t)/(\gamma + \mu)$  is defined as the average number of secondary infections caused  
 440 by a single infected individual in a fully susceptible population and measures the  
 441 intrinsic transmissibility of a pathogen.

442 When we first introduce the idea of pathogen resilience (Figure 2), we impose  
 443 sinusoidal changes to the transmission rate to account for seasonal transmission:

$$\beta(t) = b_1(1 + \theta \cos(2\pi(t - \phi)))\alpha(t), \quad (11)$$

444 where  $b_1$  represents the baseline transmission rate,  $\theta$  represents the seasonal ampli-  
 445 tude, and  $\phi$  represents the seasonal offset term. Here, we also introduce an extra  
 446 multiplicative term  $\alpha(t)$  to account for the impact of COVID-19 interventions, where  
 447  $\alpha(t) < 1$  indicates transmission reduction. Figure 2A and 2B are generated assuming  
 448  $b_1 = 3 \times (365/7 + 1/50)/\text{years}$ ,  $\theta = 0.2$ ,  $\phi = 0$ ,  $\mu = 1/50/\text{years}$ ,  $\gamma = 365/7/\text{years}$ , and  
 449  $\delta = 1/2/\text{years}$ . In Figure 2A, we impose a 50% transmission reduction for 6 months  
 450 from 2020:

$$\alpha(t) = \begin{cases} 0.5 & 2020 \leq t < 2020.5 \\ 1 & \text{otherwise} \end{cases} \quad (12)$$

451 In Figure 2B, we impose a 50% transmission reduction for 6 months from 2020 and  
 452 a permanent 10% reduction onward:

$$\alpha(t) = \begin{cases} 1 & t < 2020 \\ 0.5 & 2020 \leq t < 2020.5 \\ 0.9 & 2020.5 \leq t \end{cases} \quad (13)$$

453 In both scenarios, we simulate the SIRS model from the following initial conditions  
 454 ( $S(0) = 1/\mathcal{R}_0$ ,  $I(0) = 1 \times 10^{-6}$ , and  $R(0) = 1 - S(0) - I(0)$ ) from 1900 until 2030.

455 To measure the empirical resilience of the SIR model (Figure 2C and 2F), we  
 456 compute the normalized distance between post-intervention susceptible and logged  
 457 infected proportions and their corresponding pre-intervention values at the same time  
 458 of year:

$$\sqrt{\left(\frac{S(t) - S_{\text{pre}}(t)}{\sigma_S}\right)^2 + \left(\frac{\log I(t) - \log I_{\text{pre}}(t)}{\sigma_{\log I}}\right)^2}, \quad (14)$$

459 where  $\sigma_S$  and  $\sigma_{\log I}$  represent the standard deviation in the pre-intervention suscep-  
 460 tible and logged infected proportions. We normalize the differences in susceptible  
 461 and logged infected proportions to allow both quantities to equally contribute to the

<sup>462</sup> changes in distance from attractor. In Supplementary Materials, we also compare  
<sup>463</sup> the how the degree of seasonal transmission affects empirical resilience by varying  
<sup>464</sup>  $\theta$  from 0 to 0.4; when we assume no seasonality ( $\theta = 0$ ), we do not normalize the  
<sup>465</sup> distance because the standard deviation of pre-intervention dynamics are zero.

<sup>466</sup> Finally, we use the SIRS model to understand how underlying epidemiological  
<sup>467</sup> parameters affect pathogen resilience and link this relationship to underlying sus-  
<sup>468</sup> ceptible host dynamics. For the simple SIRS model without seasonal transmission  
<sup>469</sup> ( $\theta = 0$ ), the intrinsic resilience corresponds to:

$$-\frac{\text{Re}(\lambda)}{2} = \frac{\delta + \beta I^* + \mu}{2}. \quad (15)$$

<sup>470</sup> Here,  $I^*$  represents the prevalence values at endemic equilibrium:

$$I^* = \frac{(\delta + \mu)(\beta - (\gamma + \mu))}{\beta(\delta + \gamma + \mu)}. \quad (16)$$

<sup>471</sup> The susceptible replenishment rate is given by:

$$S_{\text{replenish}} = \frac{\mu + \delta R}{S^*}, \quad (17)$$

<sup>472</sup> where  $S^* = 1/\mathcal{R}_0$  represents the equilibrium proportion of susceptible individuals.  
<sup>473</sup> We vary the basic reproduction number  $\mathcal{R}_0$  between 1.1 to 6 and the average duration  
<sup>474</sup> of immunity  $1/\delta$  between 2 to 80 years, and compute these two quantities. In doing  
<sup>475</sup> so, we fix all other parameters:  $\mu = 1/80/\text{years}$  and  $\gamma = 365/7/\text{years}$ .

<sup>476</sup> **Supplementary Text**

<sup>477</sup> **Resilience of a stage-structured system.**

<sup>478</sup> In Figure 2G–I, we use a more realistic, stage-structured model to illustrate how  
<sup>479</sup> transient phenomena can cause the system to slow down. Specifically, we use the  
<sup>480</sup> stage-structured RSV model proposed by [22], which assumes that subsequent rein-  
<sup>481</sup> fections cause an individual to become less susceptible and transmissible than previ-  
<sup>482</sup> ous infections. The model dynamics can be described as follows:

$$\frac{dM}{dt} = \mu - (\omega + \mu)M \quad (S1)$$

$$\frac{dS_0}{dt} = \omega M - (\lambda(t) + \mu)S_0 \quad (S2)$$

$$\frac{dI_1}{dt} = \lambda(t)S_0 - (\gamma_1 + \mu)I_1 \quad (S3)$$

$$\frac{dS_1}{dt} = \gamma_1 I_1 - (\sigma_1 \lambda(t) + \mu)S_1 \quad (S4)$$

$$\frac{dI_2}{dt} = \sigma_1 \lambda(t)S_1 - (\gamma_2 + \mu)I_2 \quad (S5)$$

$$\frac{dS_2}{dt} = \gamma_2 I_2 - (\sigma_2 \lambda(t) + \mu)S_2 \quad (S6)$$

$$\frac{dI_3}{dt} = \sigma_2 \lambda(t)S_2 - (\gamma_3 + \mu)I_3 \quad (S7)$$

$$\frac{dS_3}{dt} = \gamma_3 I_3 - (\sigma_3 \lambda(t) + \mu)S_3 + \gamma_4 I_4 \quad (S8)$$

$$\frac{dI_4}{dt} = \sigma_3 \lambda(t)S_3 - (\gamma_4 + \mu)I_4 \quad (S9)$$

$$(S10)$$

<sup>483</sup> where  $M$  represents the proportion of individuals who are maternally immune;  $S_i$   
<sup>484</sup> represents the proportion of individuals who are susceptible after  $i$  prior infections;  $I_i$   
<sup>485</sup> represents the proportion of individuals who are currently (re)-infected with their  $i$ -th  
<sup>486</sup> infection;  $\mu$  represents the birth and death rates;  $1/\omega$  represents the mean duration  
<sup>487</sup> of maternal immunity;  $1/\gamma_i$  represents the mean duration of infection;  $\lambda(t)$  represents  
<sup>488</sup> the force of infection; and  $\sigma_i$  represents the reduction in susceptibility for reinfection.  
<sup>489</sup> The force of infection is modeled using a sinusoidal function:

$$\beta(t) = b_1(1 + \theta \cos(2\pi(t - \phi)))\alpha(t) \quad (S11)$$

$$\lambda(t) = \beta(I_1 + \rho_1 I_2 + \rho_2(I_3 + I_4)), \quad (S12)$$

<sup>490</sup> where  $b_1$  represents the baseline transmission rate;  $\theta$  represents the seasonal ampli-  
<sup>491</sup> tude;  $\phi$  represents the seasonal offset term;  $\alpha(t)$  represents the intervention effect;  
<sup>492</sup> and  $\rho_i$  represents the impact of immunity on transmission reduction. We use the

<sup>493</sup> following parameters to simulate the impact of interventions on epidemic dynam-  
<sup>494</sup> ics [22]:  $b_1 = 9 \times (365/10 + 1/80)/\text{years}$ ,  $\theta = 0.2$ ,  $\phi = -0.1$ ,  $\omega = 365/112/\text{years}$ ,  
<sup>495</sup>  $\gamma_1 = 365/10/\text{years}$ ,  $\gamma_2 = 365/7/\text{years}$ ,  $\gamma_3 = 365/5/\text{years}$ ,  $\sigma_1 = 0.76$ ,  $\sigma_2 = 0.6$ ,  
<sup>496</sup>  $\sigma_3 = 0.4$ ,  $\rho_1 = 0.75$ ,  $\rho_2 = 0.51$ , and  $\mu = 1/80/\text{years}$ . We assume a 50% transmission  
<sup>497</sup> reduction for 6 months from 2020:

$$\alpha(t) = \begin{cases} 0.5 & 2020 \leq t < 2020.5 \\ 1 & \text{otherwise} \end{cases} \quad (\text{S13})$$

<sup>498</sup> The model is simulated from 1900 to 2030 using the following initial conditions:  
<sup>499</sup>  $M = 0$ ,  $S_0 = 1/\mathcal{R}_0 - I_1$ ,  $I_1 = 1 \times 10^{-6}$ ,  $S_1 = 1 - 1/\mathcal{R}_0$ ,  $I_2 = 0$ ,  $S_2 = 0$ ,  $I_3 = 0$ ,  
<sup>500</sup>  $S_3 = 0$ , and  $I_4 = 0$ . For the phase plane analysis (Figure 2H) and distance analysisus  
<sup>501</sup> (Figure 2I), we rely on the average susceptibility,

$$\bar{S} = S_0 + \sigma_1 S_1 + \sigma_2 S_2 + \sigma_3 S_3, \quad (\text{S14})$$

<sup>502</sup> and total prevalence,

$$I_{\text{total}} = I_1 + I_2 + I_3 + I_4. \quad (\text{S15})$$

<sup>503</sup> These quantities are used to compute the normalized distance from the attractor, as  
<sup>504</sup> described in the main text.

## <sup>505</sup> Resilience of a multistain system.

<sup>506</sup> We use a simple two-strain model to show that a multistain host-pathogen system  
<sup>507</sup> that is coupled through cross immunity can be described by a single resilience value.  
<sup>508</sup> The model dynamics can be described as follows [20]:

$$\frac{dS}{dt} = \mu - \mu S - (\lambda_1 + \lambda_2)S + \rho_1 R_1 + \rho_2 R_2 \quad (\text{S16})$$

$$\frac{dI_1}{dt} = \lambda_1 S - (\gamma_1 + \mu)I_1 \quad (\text{S17})$$

$$\frac{dI_2}{dt} = \lambda_2 S - (\gamma_2 + \mu)I_2 \quad (\text{S18})$$

$$\frac{dR_1}{dt} = \gamma_1 I_1 - \lambda_2 \epsilon_{21} R_1 - \rho_1 R_1 + \rho_2 R - \mu R_1 \quad (\text{S19})$$

$$\frac{dR_2}{dt} = \gamma_2 I_2 - \lambda_1 \epsilon_{12} R_2 - \rho_2 R_2 + \rho_1 R - \mu R_2 \quad (\text{S20})$$

$$\frac{dJ_1}{dt} = \lambda_1 \epsilon_{12} R_2 - (\gamma_1 + \mu) J_1 \quad (\text{S21})$$

$$\frac{dJ_2}{dt} = \lambda_2 \epsilon_{21} R_1 - (\gamma_2 + \mu) J_2 \quad (\text{S22})$$

$$\frac{dR}{dt} = \gamma_1 J_1 + \gamma_2 J_2 - \rho_1 R - \rho_2 R - \mu R \quad (\text{S23})$$

where  $S$  represents the proportion of individuals who are fully susceptible to infections by both strains;  $I_1$  represents the proportion of individuals who are infected with strain 1 without prior immunity;  $I_2$  represents the proportion of individuals who are infected with strain 2 without prior immunity;  $R_1$  represents the proportion of individuals who are fully immune against strain 1 and partially susceptible to reinfection by strain 2;  $R_2$  represents the proportion of individuals who are fully immune against strain 2 and partially susceptible to reinfection by strain 1;  $J_1$  represents the proportion of individuals who are infected with strain 1 with prior immunity against strain 2;  $J_2$  represents the proportion of individuals who are infected with strain 2 with prior immunity against strain 1;  $R$  represents the proportion of individuals who are immune to infections from both strains;  $\mu$  represents the birth/death rate;  $\lambda_1$  and  $\lambda_2$  represent the force of infection from strains 1 and 2, respectively;  $\rho_1$  and  $\rho_2$  represent the waning immunity rate;  $\gamma_1$  and  $\gamma_2$  represent the recovery rate;  $\epsilon_{12}$  and  $\epsilon_{21}$  represent the susceptibility to reinfection with strains 2 and 1, respectively, given prior immunity from infection with strains 1 and 2, respectively. The force of infection is modeled as follows:

$$\beta_1 = b_1(1 + \theta_1 \sin(2\pi(t - \phi_1)))\alpha(t) \quad (\text{S24})$$

$$\beta_2 = b_2(1 + \theta_2 \sin(2\pi(t - \phi_2)))\alpha(t) \quad (\text{S25})$$

$$\lambda_1 = \beta_1(I_1 + J_1) \quad (\text{S26})$$

$$\lambda_2 = \beta_2(I_2 + J_2) \quad (\text{S27})$$

In Supplementary Figures S2–S4, we assume the following parameters:  $b_1 = 2 \times 52/\text{years}$ ,  $b_2 = 4 \times 52/\text{years}$ ,  $\phi_1 = \phi_2 = 0$ ,  $\epsilon_{12} = 0.9$ ,  $\epsilon_{21} = 0.5$ ,  $\gamma_1 = \gamma_2 = 52/\text{years}$ ,  $\rho_1 = \rho_2 = 1/\text{years}$ , and  $\mu = 1/70/\text{years}$ . For all simulations, we assume a 50% transmission reduction for 6 months from 2020:

$$\alpha(t) = \begin{cases} 0.5 & 2020 \leq t < 2020.5 \\ 1 & \text{otherwise} \end{cases} \quad (\text{S28})$$

The seasonal amplitude  $\theta$  is varied from 0 to 0.4. All simulations are ran from 1900 to 2030 from the following initial conditions:  $S(0) = 1 - 2 \times 10^{-6}$ ,  $I_1(0) = 1 \times 10^{-6}$ ,  $I_2(0) = 1 \times 10^{-6}$ ,  $R_1(0) = 0$ ,  $R_2(0) = 0$ ,  $J_1(0) = 0$ ,  $J_2(0) = 0$ , and  $R(0) = 0$ .

For this, we consider three different scenarios for measuring pathogen resilience: (1) we only have information about strain 1, (2) we only have information about strain 2, and (3) we are unable to distinguish the differences between strains. In the first two scenarios (see panels A–C for strain 1 and panels D–F for strain 2), we consider the dynamics of average susceptibility for each strain and total prevalence:

$$\bar{S}_1 = S + \epsilon_{12}R_2 \quad (\text{S29})$$

$$\hat{I}_1 = I_1 + J_1 \quad (\text{S30})$$

$$\bar{S}_2 = S + \epsilon_{21}R_1 \quad (\text{S31})$$

$$\hat{I}_2 = I_2 + J_2 \quad (\text{S32})$$

<sup>537</sup> In the third scenario (panels G–I), we consider the dynamics of total susceptible  
<sup>538</sup> and infected population:

$$\hat{S} = S + R_2 + R_1 \quad (\text{S33})$$

$$\hat{I} = I_1 + J_1 + I_2 + J_2 \quad (\text{S34})$$

$$(\text{S35})$$

<sup>539</sup> These quantities are used to compute the normalized distance from the attractor, as  
<sup>540</sup> described in the main text.

## <sup>541</sup> Estimating intrinsic resilience using mechanistic model

<sup>542</sup> We test whether we can reliably estimate the intrinsic resilience of a system by fitting  
<sup>543</sup> a mechanistic model. Specifically, we simulate case time series from stochastic SIRS  
<sup>544</sup> and two-strain models and fit a simple, deterministic SIRS model using a Bayesian  
<sup>545</sup> framework.

<sup>546</sup> First, we describe the simulation set up. The stochastic SIRS model can be  
<sup>547</sup> written as follows:

$$\beta(t) = \mathcal{R}_0 \left( 1 + \theta \cos \left( \frac{2\pi t}{364} \right) \right) \alpha(t)(1 - \exp(-\gamma)) \quad (\text{S36})$$

$$\text{FOI}(t) = \beta(t)I(t - \Delta t)/N \quad (\text{S37})$$

$$B(t) \sim \text{Poisson}(\mu N) \quad (\text{S38})$$

$$\Delta S(t) \sim \text{Binom}(S(t - \Delta t), 1 - \exp(-(\text{FOI}(t) + \mu)\Delta t)) \quad (\text{S39})$$

$$N_{SI}(t) \sim \text{Binom}\left(\Delta S(t), \frac{\text{FOI}(t)}{\text{FOI}(t) + \mu}\right) \quad (\text{S40})$$

$$\Delta I(t) \sim \text{Binom}(I(t - \Delta t), 1 - \exp(-(\gamma + \mu)\Delta t)) \quad (\text{S41})$$

$$N_{IR}(t) \sim \text{Binom}\left(\Delta I(t), \frac{\gamma}{\gamma + \mu}\right) \quad (\text{S42})$$

$$\Delta R(t) \sim \text{Binom}(R(t - \Delta t), 1 - \exp(-(\delta + \mu)\Delta t)) \quad (\text{S43})$$

$$N_{RS}(t) \sim \text{Binom}\left(\Delta R(t), \frac{\delta}{\delta + \mu}\right) \quad (\text{S44})$$

$$S(t) = S(t - \Delta t) + N_{RS}(t) + B(t) - \Delta S(t) \quad (\text{S45})$$

$$I(t) = I(t - \Delta t) + N_{SI}(t) - \Delta I(t) \quad (\text{S46})$$

$$R(t) = R(t - \Delta t) + N_{IR}(t) - \Delta R(t) \quad (\text{S47})$$

<sup>548</sup> where FOI represent the force of infection;  $N_{ij}$  represent the number of individuals  
<sup>549</sup> moving from compartment  $i$  to  $j$  on a given day; and  $B(t)$  represents the number  
<sup>550</sup> of new births. We simulate the model on a daily scale—assuming 364 days in a  
<sup>551</sup> year so that it can be evenly grouped into 52 weeks—with the following parameters:  
<sup>552</sup>  $\mathcal{R}_0 = 3$ ,  $\theta = 0.1$ ,  $\gamma = 1/7/\text{days}$ ,  $\delta = 1/(364 \times 2)/\text{days}$ ,  $\mu = 1/(364 \times 50)/\text{days}$ , and

<sup>553</sup>  $N = 1 \times 10^8$ . The model is simulated from 1900 to 2030 assuming  $S(0) = N/3$ ,  
<sup>554</sup>  $I(0) = 100$ , and  $R(0) = N - S(0) - I(0)$ . The observed incidence from the model is  
<sup>555</sup> then simulated as follows:

$$C(t) = \text{Beta} - \text{Binom}(N_{SI}(t), \rho, k), \quad (\text{S48})$$

<sup>556</sup> where  $\rho$  represents the reporting probability and  $k$  represents the overdispersion pa-  
<sup>557</sup> rameter of beta-binomial distribution. We assume  $\rho = 0.002$  (i.e., 0.2% probability)  
<sup>558</sup> and  $k = 1000$ .

<sup>559</sup> The stochastic two-strain model can be written as follows:

$$\beta_1(t) = b_1 \left( 1 + \theta_1 \cos \left( \frac{2\pi(t - \phi_1)}{364} \right) \right) \alpha(t) \quad (\text{S49})$$

$$\beta_2(t) = b_2 \left( 1 + \theta_2 \cos \left( \frac{2\pi(t - \phi_2)}{364} \right) \right) \alpha(t) \quad (\text{S50})$$

$$\text{FOI}_1(t) = \beta_1(t)(I_1(t - \Delta t) + J_1(t - \Delta t))/N \quad (\text{S51})$$

$$\text{FOI}_2(t) = \beta_2(t)(I_2(t - \Delta t) + J_2(t - \Delta t))/N \quad (\text{S52})$$

$$B(t) \sim \text{Poisson}(\mu N) \quad (\text{S53})$$

$$\Delta S(t) \sim \text{Binom}(S(t - \Delta t), 1 - \exp(-(\text{FOI}_1(t) + \text{FOI}_2(t) + \mu)\Delta t)) \quad (\text{S54})$$

$$N_{SI_1}(t) \sim \text{Binom}\left(\Delta S(t), \frac{\text{FOI}_1(t)}{\text{FOI}_1(t) + \text{FOI}_2(t) + \mu}\right) \quad (\text{S55})$$

$$N_{SI_2}(t) \sim \text{Binom}\left(\Delta S(t), \frac{\text{FOI}_2(t)}{\text{FOI}_1(t) + \text{FOI}_2(t) + \mu}\right) \quad (\text{S56})$$

$$\Delta I_1(t) \sim \text{Binom}(I_1(t - \Delta t), 1 - \exp(-(\gamma_1 + \mu)\Delta t)) \quad (\text{S57})$$

$$N_{I_1 R_1}(t) \sim \text{Binom}\left(\Delta I_1(t), \frac{\gamma_1}{\gamma_1 + \mu}\right) \quad (\text{S58})$$

$$\Delta I_2(t) \sim \text{Binom}(I_2(t - \Delta t), 1 - \exp(-(\gamma_2 + \mu)\Delta t)) \quad (\text{S59})$$

$$N_{I_2 R_2}(t) \sim \text{Binom}\left(\Delta I_2(t), \frac{\gamma_2}{\gamma_2 + \mu}\right) \quad (\text{S60})$$

$$\Delta R_1(t) \sim \text{Binom}(R_1(t - \Delta t), 1 - \exp(-(\epsilon_{21}\text{FOI}_2(t) + \rho_1 + \mu)\Delta t)) \quad (\text{S61})$$

$$N_{R_1 S}(t) \sim \text{Binom}\left(\Delta R_1(t), \frac{\rho_1}{\epsilon_{21}\text{FOI}_2(t) + \rho_1 + \mu}\right) \quad (\text{S62})$$

$$N_{R_1 J_2}(t) \sim \text{Binom}\left(\Delta R_1(t), \frac{\epsilon_{21}\text{FOI}_2(t)}{\epsilon_{21}\text{FOI}_2(t) + \rho_1 + \mu}\right) \quad (\text{S63})$$

$$\Delta R_2(t) \sim \text{Binom}(R_2(t - \Delta t), 1 - \exp(-(\epsilon_{12}\text{FOI}_1(t) + \rho_2 + \mu)\Delta t)) \quad (\text{S64})$$

$$N_{R_2 S}(t) \sim \text{Binom}\left(\Delta R_2(t), \frac{\rho_2}{\epsilon_{12}\text{FOI}_1(t) + \rho_2 + \mu}\right) \quad (\text{S65})$$

$$N_{R_2 J_1}(t) \sim \text{Binom}\left(\Delta R_2(t), \frac{\epsilon_{12}\text{FOI}_1(t)}{\epsilon_{12}\text{FOI}_1(t) + \rho_2 + \mu}\right) \quad (\text{S66})$$

$$\Delta J_1(t) \sim \text{Binom}(J_1(t - \Delta t), 1 - \exp(-(\gamma_1 + \mu)\Delta t)) \quad (\text{S67})$$

$$N_{J_1R}(t) \sim \text{Binom}\left(\Delta J_1(t), \frac{\gamma_1}{\gamma_1 + \mu}\right) \quad (\text{S68})$$

$$\Delta J_2(t) \sim \text{Binom}(J_2(t - \Delta t), 1 - \exp(-(\gamma_2 + \mu)\Delta t)) \quad (\text{S69})$$

$$N_{J_2R}(t) \sim \text{Binom}\left(\Delta J_2(t), \frac{\gamma_2}{\gamma_2 + \mu}\right) \quad (\text{S70})$$

$$\Delta R(t) \sim \text{Binom}(R(t - \Delta t), 1 - \exp(-(\rho_1 + \rho_2 + \mu)\Delta t)) \quad (\text{S71})$$

$$N_{RR_1}(t) \sim \text{Binom}\left(\Delta R(t), \frac{\rho_1}{\rho_1 + \rho_2 + \mu}\right) \quad (\text{S72})$$

$$N_{RR_2}(t) \sim \text{Binom}\left(\Delta R(t), \frac{\rho_2}{\rho_1 + \rho_2 + \mu}\right) \quad (\text{S73})$$

$$S(t) = S(t - \Delta t) - \Delta S(t) + B(t) + N_{R_1S}(t) + N_{R_2S}(t) \quad (\text{S74})$$

$$I_1(t) = I_1(t - \Delta t) - \Delta I_1(t) + N_{SI_1}(t) \quad (\text{S75})$$

$$I_2(t) = I_2(t - \Delta t) - \Delta I_2(t) + N_{SI_2}(t) \quad (\text{S76})$$

$$R_1(t) = R_1(t - \Delta t) - \Delta R_1(t) + N_{I_1R_1}(t) + N_{RR_1}(t) \quad (\text{S77})$$

$$R_2(t) = R_2(t - \Delta t) - \Delta R_2(t) + N_{I_2R_2}(t) + N_{RR_2}(t) \quad (\text{S78})$$

$$J_1(t) = J_1(t - \Delta t) - \Delta J_1(t) + N_{R_2J_1}(t) \quad (\text{S79})$$

$$J_2(t) = J_2(t - \Delta t) - \Delta J_2(t) + N_{R_1J_2}(t) \quad (\text{S80})$$

$$R(t) = R(t - \Delta t) - \Delta R(t) + N_{J_1R}(t) + N_{J_2R}(t) \quad (\text{S81})$$

560 We simulate the model on a daily scale with previously estimated parameters for the  
 561 RSV-HMPV interaction [20]:  $b_1 = 1.7/\text{weeks}$ ,  $b_2 = 1.95/\text{weeks}$ ,  $\theta_1 = 0.4$ ,  $\theta_2 = 0.3$ ,  
 562  $\phi_1 = 0.005 \times 7/364$ ,  $\phi_2 = 4.99 \times 7/364$ ,  $\epsilon_{12} = 0.92$ ,  $\epsilon_{21} = 0.45$ ,  $\gamma_1 = 1/10/\text{days}$ ,  
 563  $\gamma_2 = 1/10/\text{days}$ ,  $\rho_1 = 1/364/\text{days}$ ,  $\rho_2 = 1/364/\text{days}$ ,  $\mu = 1/(70 \times 364)/\text{days}$ , and  
 564  $N = 1 \times 10^8$ . The model is simulated from 1900 to 2030 assuming  $S(0) = N - 200$ ,  
 565  $I_1(0) = 100$ ,  $I_2(0) = 100$ ,  $R_1(0) = 0$ ,  $R_2(0) = 0$ ,  $J_1(0) = 0$ ,  $J_2(0) = 0$ , and  $R(0) = 0$ .  
 566 The observed incidence for each strain is then simulated as follows:

$$C_1(t) = \text{Beta} - \text{Binom}(N_{SI_1}(t) + N_{R_2J_1}, \rho, k), \quad (\text{S82})$$

$$C_2(t) = \text{Beta} - \text{Binom}(N_{SI_2}(t) + N_{R_1J_2}, \rho, k), \quad (\text{S83})$$

567 where  $\rho$  represents the reporting probability and  $k$  represents the overdispersion pa-  
 568 rameter of beta-binomial distribution. We assume  $\rho = 0.002$  (i.e., 0.2% probability)  
 569 and  $k = 500$ . We also consider the total incidence:  $C_{\text{total}}(t) = C_1(t) + C_2(t)$ .

570 For both models, we consider a more realistic challenges in intervention effects  
 571  $\alpha(t)$  to challenge our ability to estimate the intervention effects. Thus, we assume  
 572 a 40% transmission reduction for 3 months from March 2020, followed by a 10%  
 573 transmission reduction for 6 months, 20% transmission reduction for 3 months, and

574 a final return to normal levels:

$$\alpha(t) = \begin{cases} 1 & t < 2020.25 \\ 0.6 & 2020.25 \leq t < 2020.5 \\ 0.9 & 2020.5 \leq t < 2021 \\ 0.8 & 2021 \leq t < 2021.25 \\ 1 & 2021.25 \leq t \end{cases}. \quad (\text{S84})$$

575 For all simulations, we truncate the time series from the beginning of 2014 to the  
576 end of 2023 and aggregate them into weekly cases.

577 To infer intrinsic resilience from time series, we fit a simple discrete time, deter-  
578 ministic SIRS model [12]:

$$\Delta t = 1 \text{ week} \quad (\text{S85})$$

$$\text{FOI}(t) = \beta(t)(I(t - \Delta t) + \omega)/N \quad (\text{S86})$$

$$\Delta S(t) = [1 - \exp(-(\text{FOI}(t) + \mu)\Delta t)] S(t - \Delta t) \quad (\text{S87})$$

$$N_{SI}(t) = \frac{\text{FOI}(t)\Delta S(t)}{\text{FOI}(t) + \mu} \quad (\text{S88})$$

$$\Delta I(t) = [1 - \exp(-(\gamma + \mu)\Delta t)] I(t - \Delta t) \quad (\text{S89})$$

$$N_{IR}(t) = \frac{\gamma \Delta I(t)}{\gamma + \mu} \quad (\text{S90})$$

$$\Delta R(t) = [1 - \exp(-(\nu + \mu)\Delta t)] R(t - \Delta t) \quad (\text{S91})$$

$$N_{RS}(t) = \frac{\nu \Delta R(t)}{\nu + \mu} \quad (\text{S92})$$

$$S(t) = S(t - \Delta t) + \mu S - \Delta S(t) + N_{RS}(t) \quad (\text{S93})$$

$$I(t) = I(t - \Delta t) - \Delta I(t) + N_{SI}(t) \quad (\text{S94})$$

$$R(t) = R(t - \Delta t) - \Delta R(t) + N_{IR}(t) \quad (\text{S95})$$

579 where we include an extra term  $\omega$  to account for external infections. Although actual  
580 simulations do not include any external infections, we found that including this term  
581 generally helped with model convergence in previous analyses [12]. The transmission  
582 rate is divided into a seasonal term  $\beta_{\text{seas}}(t)$  (repeated every year) and intervention  
583 term  $\alpha(t)$ , which are estimated jointly:

$$\beta(t) = \beta_{\text{seas}}(t)\alpha(t), \quad (\text{S96})$$

584 where  $\alpha < 1$  corresponds to reduction in transmission due to intervention effects. To  
585 constrain the smoothness of  $\beta_{\text{seas}}(t)$ , we impose cyclic, random-walk priors:

$$\beta_{\text{seas}}(t) \sim \text{Normal}(\beta_{\text{seas}}(t - 1), \sigma) \quad t = 2 \dots 52 \quad (\text{S97})$$

$$\beta_{\text{seas}}(1) \sim \text{Normal}(\beta_{\text{seas}}(52), \sigma) \quad (\text{S98})$$

586 [SWP: I noticed that I forgot to put a prior on  $\sigma$  so need to re-do this but won't  
 587 change the results.] We fix  $\alpha(t) = 1$  for all  $t < 2020$  and estimate  $\alpha$  assuming a  
 588 normal prior:

$$\alpha \sim \text{Normal}(1, 0.25). \quad (\text{S99})$$

589 We assume weakly informative priors on  $\omega$  and  $\tau$ :

$$\omega \sim \text{Normal}(0, 200) \tau \sim \text{Normal}(104, 26) \quad (\text{S100})$$

590 We assume that the true birth/death rates, population sizes, and recovery rates are  
 591 known. We note, however, that assuming  $\gamma = 1/\text{week}$  actually correspond to a  
 592 mean infectious period of 1.6 weeks, which is much longer than the true value; this  
 593 approximation allows us to test whether we can still robustly estimate the intrinsic  
 594 resilience given parameters mis-specification. Initial conditions are estimated with  
 595 following priors:

$$S(0) = Ns(0) \quad (\text{S101})$$

$$I(0) = Ni(0) \quad (\text{S102})$$

$$s(0) \sim \text{Uniform}(0, 1) \quad (\text{S103})$$

$$i(0) \sim \text{Half-Normal}(0, 0.001) \quad (\text{S104})$$

596 Finally, the Observation model is specified as follows:

$$\text{Cases}(t) \sim \text{Negative-Binomial}(\rho N_{SI}(t), \phi) \quad (\text{S105})$$

$$\rho \sim \text{Half-Normal}(0, 0.02) \quad (\text{S106})$$

$$\phi \sim \text{Half-Normal}(0, 10) \quad (\text{S107})$$

597 where  $\rho$  represents the reporting probability and  $\phi$  represents the negative binomial  
 598 overdispersion parameter.

599 The model is fitted to four separate time series: (1) incidence time series from  
 600 the SIRS model, (2) incidence time series for strain 1 from the two-strain model,  
 601 (3) incidence time series for strain 2 from the two-strain model, and (4) combined  
 602 incidence time series for strains 1 and 2 from the two-strain model. The model was  
 603 fitted using rstan [28, 29]. The resulting posterior distribution was used to calculate  
 604 the intrinsic resilience of the seasonally unforced system with the same parameters;  
 605 eigenvalues of the discrete-time SIR model were computed by numerically finding  
 606 the equilibrium and calculating the Jacobian matrix.

## 607 **Validations for window-selection criteria**

608 We use stochastic SIRS simulations to validate the window-selection criteria that we  
 609 use for the linear regression for estimating empirical resilience. For each simulation,  
 610 we begin by generating a random intervention  $\alpha(t)$  from random set of parameters.  
 611 First, we draw the duration of intervention  $\tau_{\text{np}}^*$  from a uniform distribution between

612 0.5 and 3.5 years. Then, we draw independent normal variables  $z_i$  of length  $\lfloor 364\tau_{\text{npi}} \rfloor$   
 613 with a standard deviation of 0.02 and take a reverse cumulative sum to obtain a  
 614 realistic shape for the intervention:

$$x_n = 1 + \sum_{i=n}^{\lfloor 364\tau_{\text{npi}} \rfloor} z_i, \quad n = 1, \dots, \lfloor 364\tau_{\text{npi}} \rfloor. \quad (\text{S108})$$

615 We repeat this random generation process until less than 10% of  $x_n$  exceeds 1. Then,  
 616 we set any values that are above 1 or below 0 as 1 and 0, respectively. Then, we  
 617 randomly draw the minimum transmission during intervention  $\alpha_{\min}$  from a uniform  
 618 distribution between 0.5 and 0.7 and scale  $x_n$  to have a minimum of  $\alpha_{\min}$ :

$$x_{\text{scale},n} = \alpha_{\min} + (1 - \alpha_{\min}) \times \frac{x_n - \min x_n}{1 - \min x_n}. \quad (\text{S109})$$

619 This allows us to simulate a realistically shaped interventions:

$$\alpha(t) = \begin{cases} 1 & t < 2020 \\ x_{\text{scale},364(t-2020)} & 2020 \leq t < 2020 + \tau_{\text{npi}} \\ 1 & \tau_{\text{npi}} \leq t \end{cases}. \quad (\text{S110})$$

620 Given this intervention function, we draw  $\mathcal{R}_0$  from a uniform distribution between 1.5  
 621 and 3 and the mean duration of immunity  $1/\delta$  from a uniform distribution between  
 622 0.5 and 2. Then, we simulate the stochastic SIRS model from  $S(0) = 10^8/\mathcal{R}_0$  and  
 623  $I(0) = 100$  from 1990 to 2025 and truncate the time series to 2014–2025; if the  
 624 epidemic becomes extinct before the end of simulation, we discard that simulation  
 625 and start over from the intervention generation step. We then apply the window  
 626 selection criteria described in the main text to compute the empirical resilience and  
 627 compare it against the intrinsic resilience of the seasonally unforced system. We also  
 628 compare this with the naive approach that uses the entire distance-from-attractor  
 629 time series, starting from the maximum distance. We repeat this procedure 500  
 630 times and quantify the correlation between empirical and intrinsic resilience estimates  
 631 across two approaches.

# Supplementary Figures

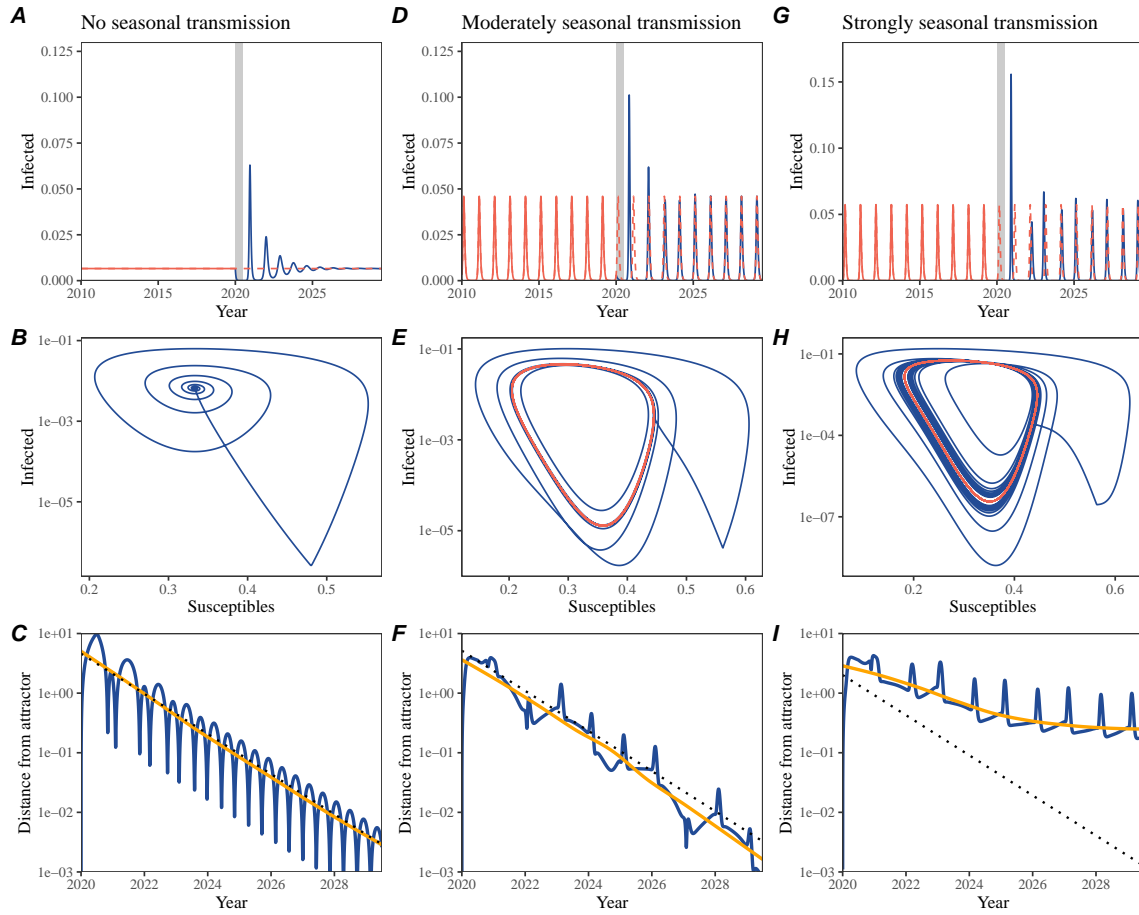


**Figure S1: Impact of seasonal transmission on pathogen resilience.** (A, D, G) Simulated epidemic trajectories using the SIRS model without seasonal forcing (A), with seasonal forcing of amplitude of 0.2 (D), and with seasonal forcing of amplitude of 0.2 (G). Red and blue solid lines represent epidemic dynamics before and after interventions are introduced, respectively. Red dashed lines represent counterfactual epidemic dynamics in the absence of interventions. Gray regions indicate the duration of interventions. (B, E, H) Phase plane representation of the corresponding model. Red and blue solid lines represent epidemic trajectories on an SI phase plane before and after interventions are introduced, respectively. (C, F, I) Changes in logged distance from attractor over time. Blue lines represent the logged distance from attractor. Orange lines represent the locally estimated scatterplot smoothing (LOESS) fits to the logged distance from attractor. Dotted lines are superimposed as a comparison to have the same slope as the intrinsic resilience of the seasonally unforced system.

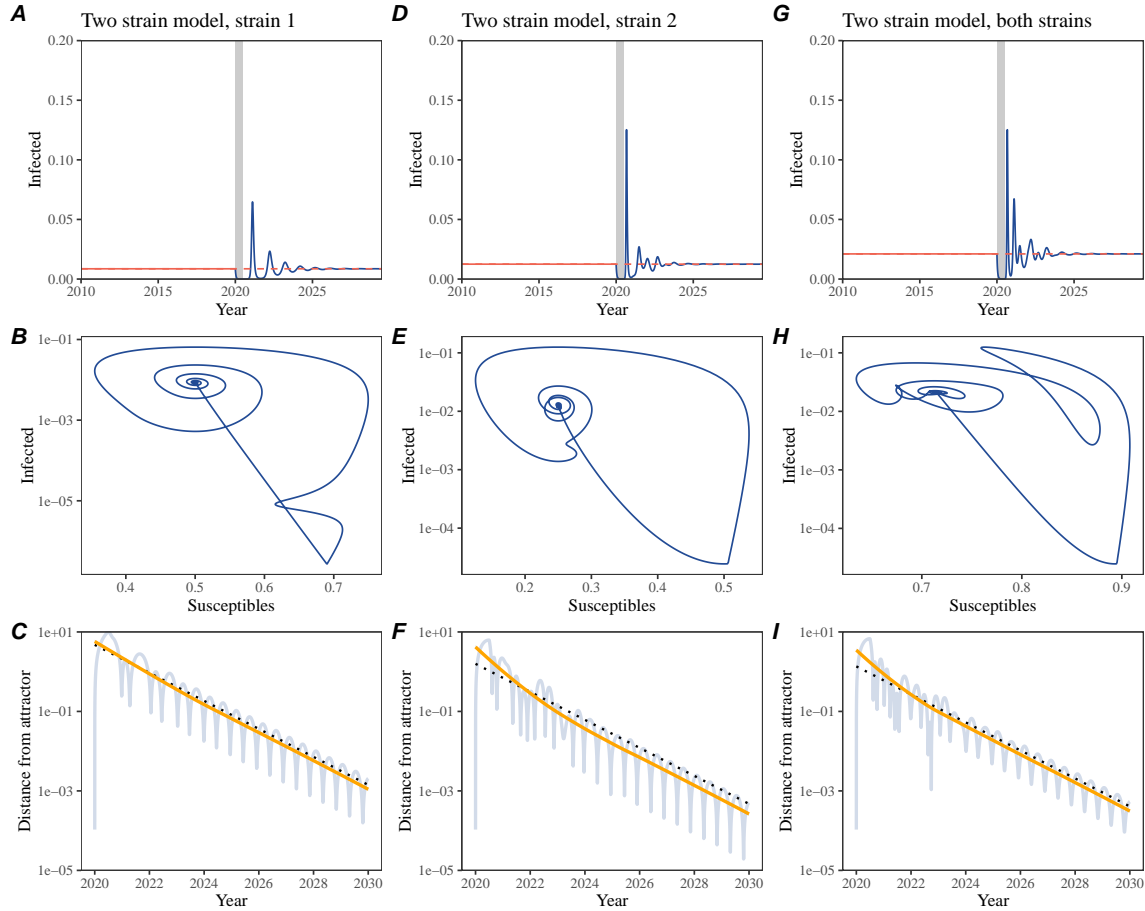


**Figure S2: Conceptual framework for measuring pathogen resilience following NPIs for a multi-strain system without seasonal forcing.** (A, D, G) Simulated epidemic trajectories using a multi-strain system without seasonal forcing. Red and blue solid lines represent epidemic dynamics before and after interventions are introduced, respectively. Red dashed lines represent counterfactual epidemic dynamics in the absence of interventions. Gray regions indicate the duration of interventions. (B, E, H) Phase plane representation of the corresponding model. Red and blue solid lines represent epidemic trajectories on an SI phase plane before and after interventions are introduced, respectively. (C, F, I) Changes in logged distance from attractor over time. Blue lines represent the logged distance from attractor. Orange lines represent the locally estimated scatterplot smoothing (LOESS) fits to the logged distance from attractor. Dotted lines are superimposed as a comparison to have the same slope as the intrinsic resilience of the seasonally unforced system.

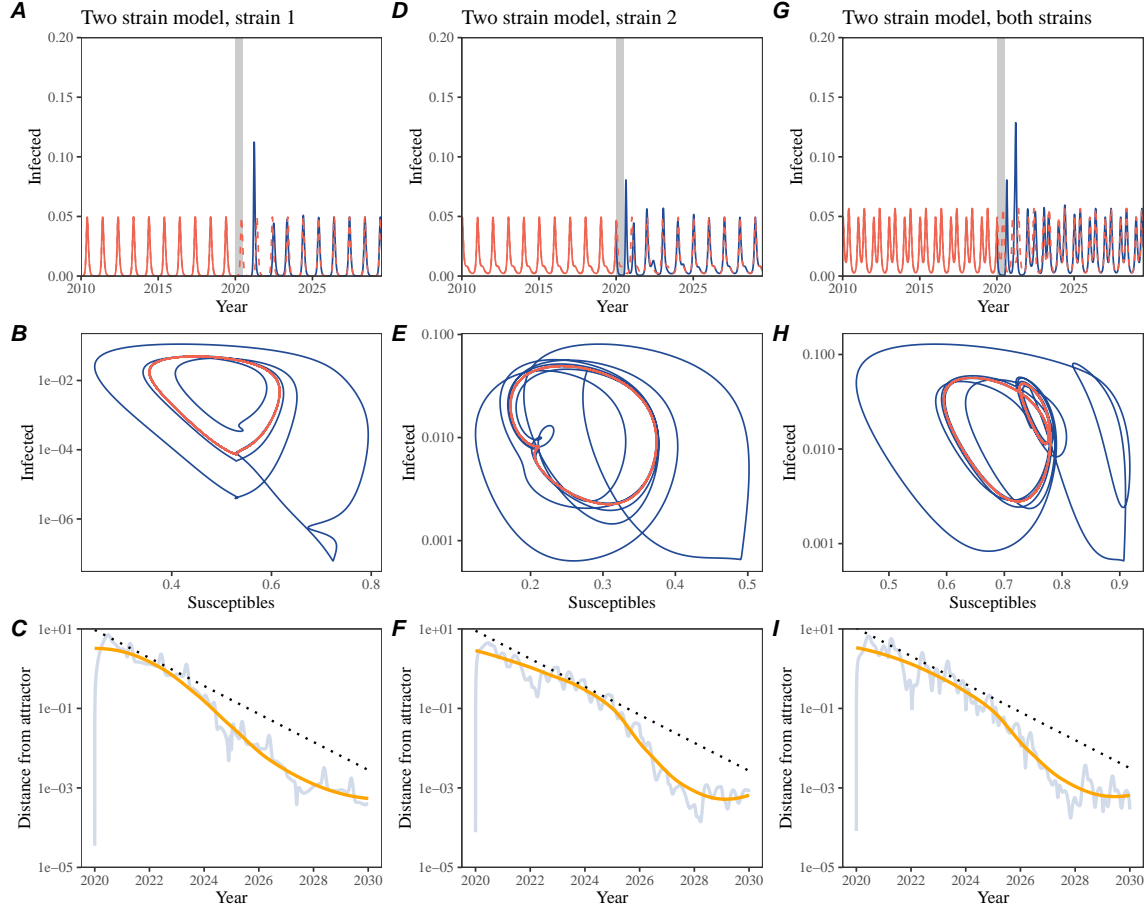


**Figure S3: Conceptual framework for measuring pathogen resilience following NPIs for a multi-strain system with seasonal forcing.** (A, D, G) Simulated epidemic trajectories using a multi-strain system with seasonal forcing (amplitude of 0.2). Red and blue solid lines represent epidemic dynamics before and after interventions are introduced, respectively. Red dashed lines represent counterfactual epidemic dynamics in the absence of interventions. Gray regions indicate the duration of interventions. (B, E, H) Phase plane representation of the corresponding model. Red and blue solid lines represent epidemic trajectories on an SI phase plane before and after interventions are introduced, respectively. (C, F, I) Changes in logged distance from attractor over time. Blue lines represent the logged distance from attractor. Orange lines represent the locally estimated scatterplot smoothing (LOESS) fits to the logged distance from attractor. Dotted lines are superimposed as a comparison to have the same slope as the intrinsic resilience of the seasonally unforced system.

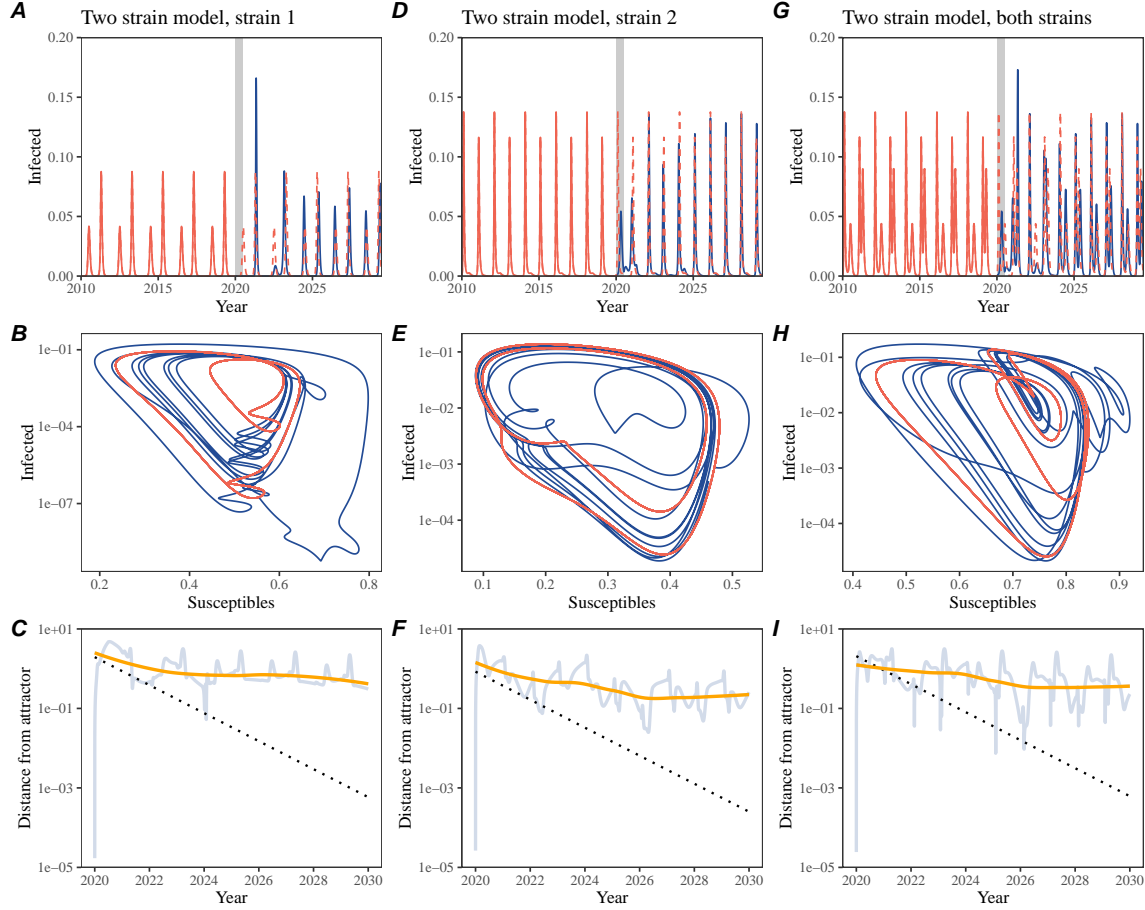


**Figure S4: Conceptual framework for measuring pathogen resilience following NPIs for a multi-strain system with strong seasonal forcing.** (A, D, G) Simulated epidemic trajectories using a multi-strain system with seasonal forcing (amplitude of 0.4). Red and blue solid lines represent epidemic dynamics before and after interventions are introduced, respectively. Red dashed lines represent counterfactual epidemic dynamics in the absence of interventions. Gray regions indicate the duration of interventions. (B, E, H) Phase plane representation of the corresponding model. Red and blue solid lines represent epidemic trajectories on an SI phase plane before and after interventions are introduced, respectively. (C, F, I) Changes in logged distance from attractor over time. Blue lines represent the logged distance from attractor. Orange lines represent the locally estimated scatterplot smoothing (LOESS) fits to the logged distance from attractor. Dotted lines are superimposed as a comparison to have the same slope as the intrinsic resilience of the seasonally unforced system.

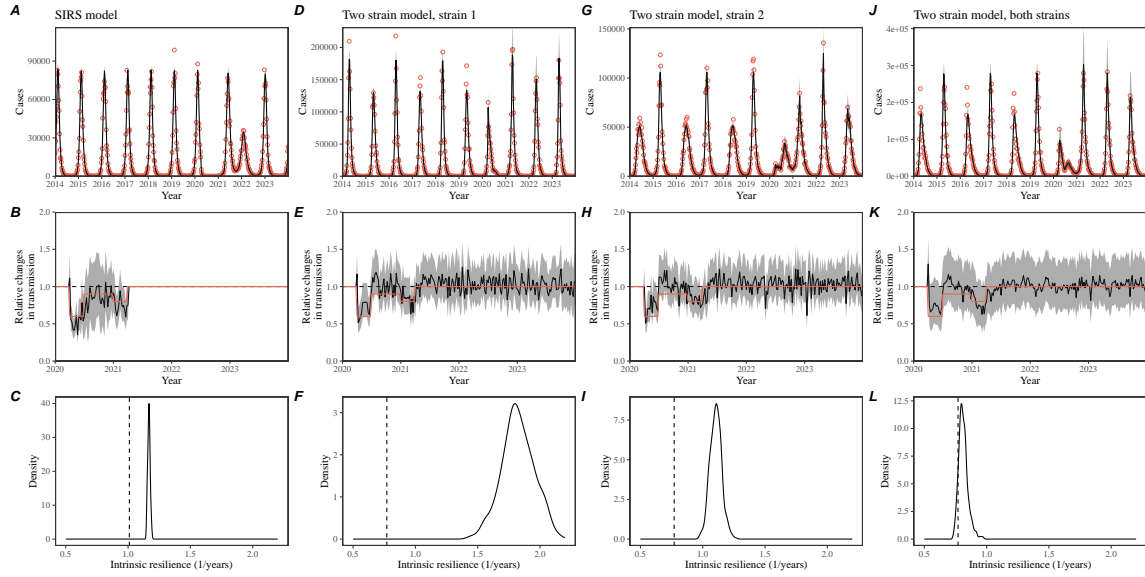


**Figure S5: Mechanistic model fits to simulated data and inferred intrinsic resilience.** (A, D, G, J) Simulated case time series from corresponding models (red) and SIRS model fits (black). (B, E, H, K) Assumed changes in transmission due to COVID-19 interventions (red) and estimated changes from the SIRS model (black). Solid lines and shaded regions represent fitted posterior median and 95% credible intervals. (C, F, I, L) True intrinsic resilience of the seasonally unforced system (vertical lines) and the posterior distribution of the inferred intrinsic resilience from the SIRS model (density plots).

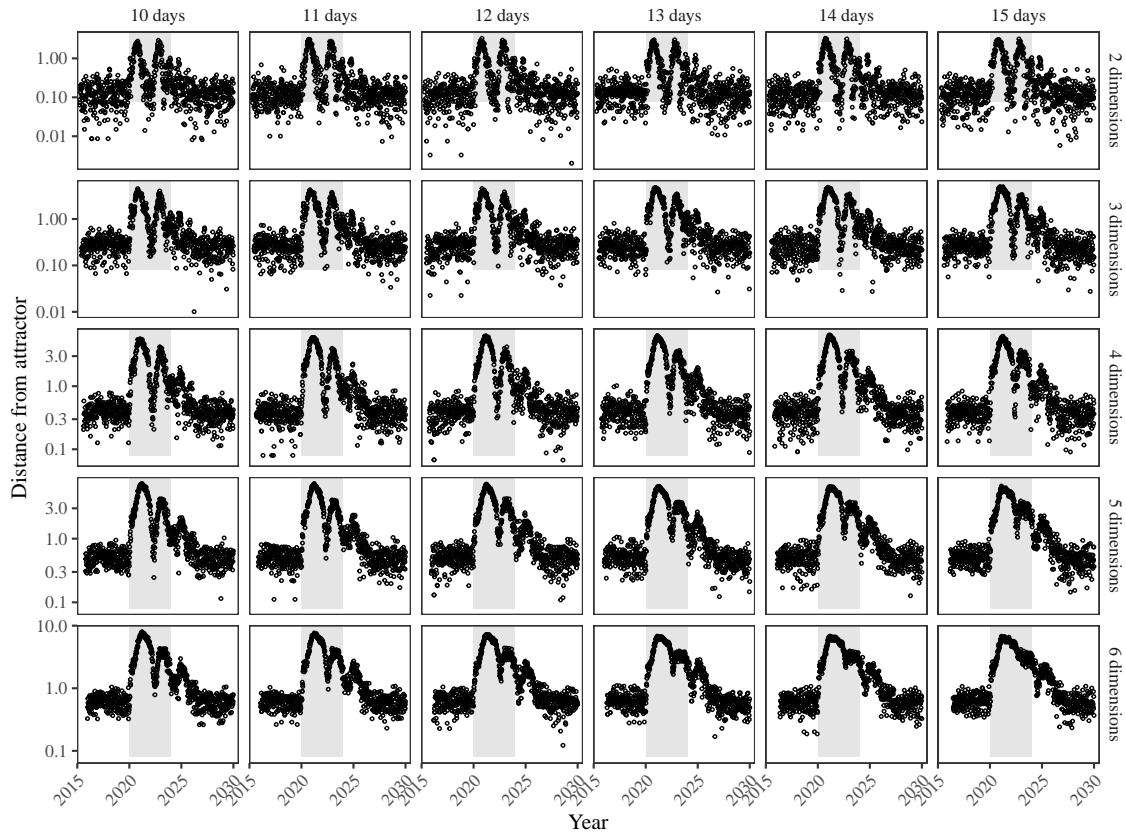


**Figure S6: Sensitivity of the distance from attractor to choices about embedding lags and dimensions.** Sensitivity analysis for the distance-from-attractor time series shown in Figure 3E in the main text by varying the embedding lag between 10–15 days and embedding dimensions between 2–6 dimensions.

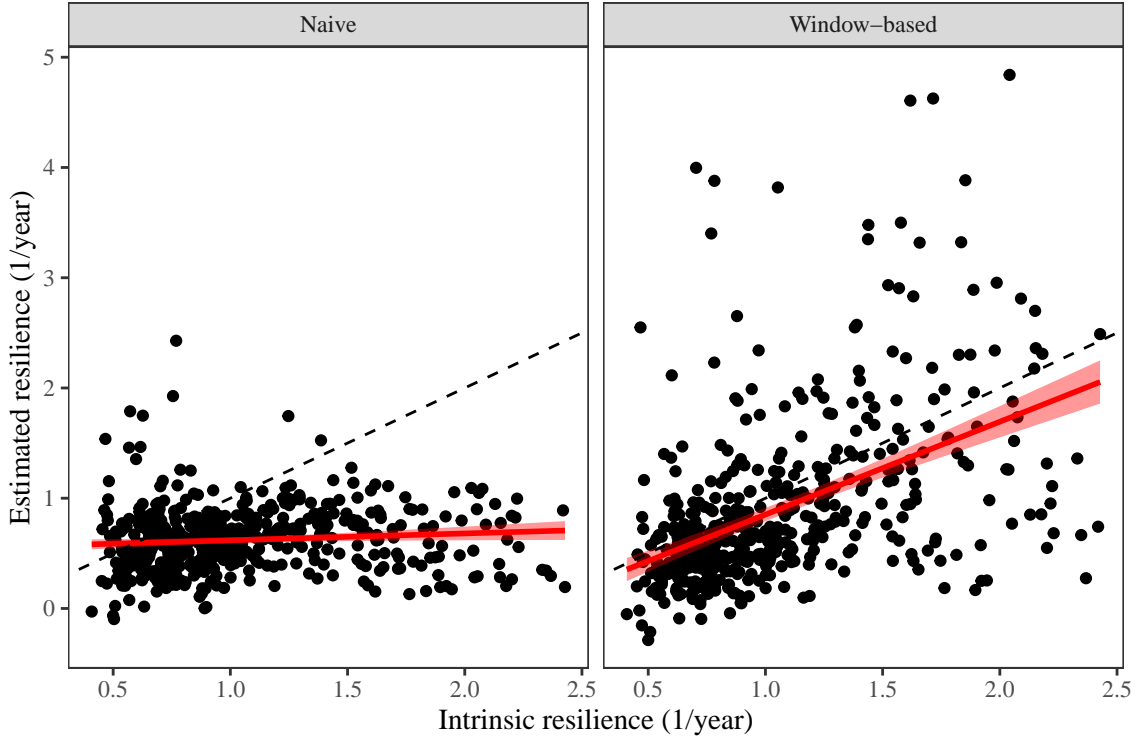


**Figure S7: Impact of fitting window selection on the estimation of empirical resilience.** We simulate 500 epidemics using stochastic SIRS model with randomly drawn parameters and randomly generated intervention impacts. For each simulation, we reconstruct the empirical attractor based on the approach outlined in Figure 3 and estimate the distance from attractor. The naive approach fits a linear regression on a log scale, starting from the maximum distance until the end of the time series. The window-based approach tries to select an appropriate window by smoothing the distance estimates and finding a time period when the smoothed time series crosses pre-determined threshold, relatively to the maximum distance; then, a linear regression is fitted by using the raw distance within this time period.

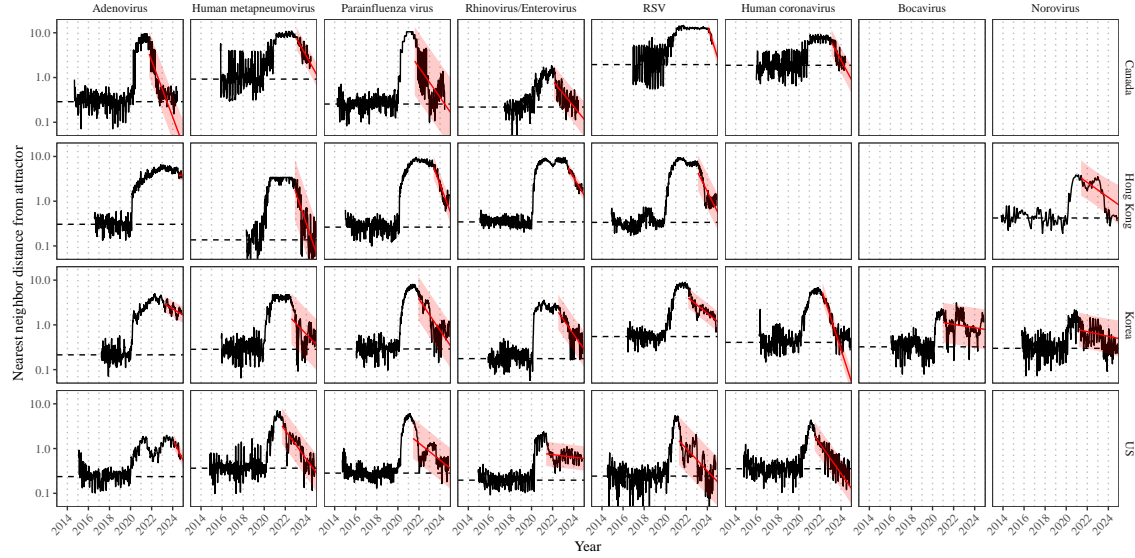


**Figure S8: Estimated time series of distance from attractor for each pathogen across Canada, Hong Kong, Korea, and the US.** Black lines represent the estimated distance from attractor. Red lines and shaded regions represent the linear regression fits and corresponding 95% confidence intervals. Dashed lines represent the average of the pre-pandemic nearest neighbor distances.

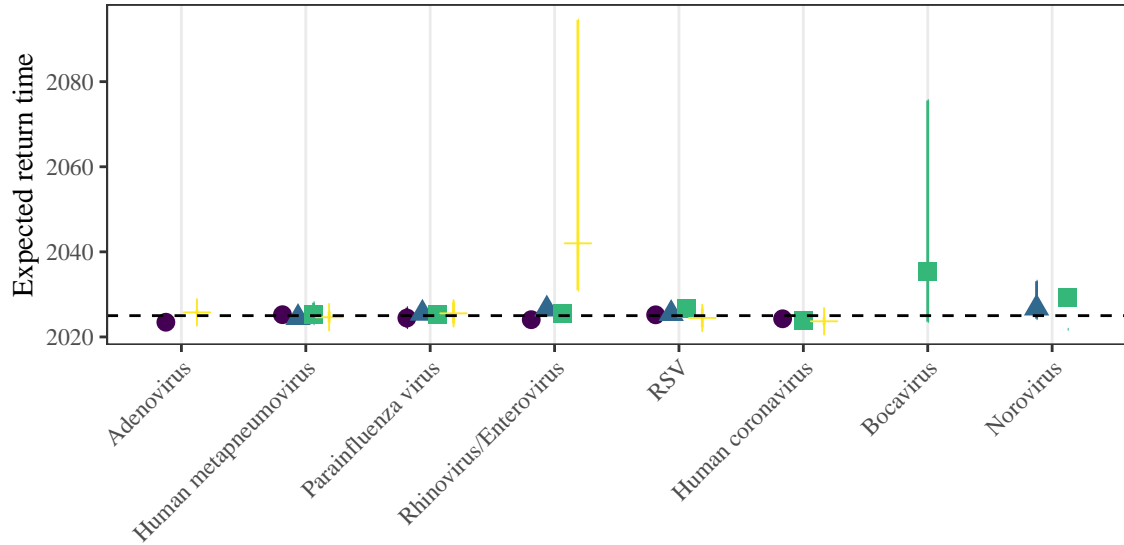
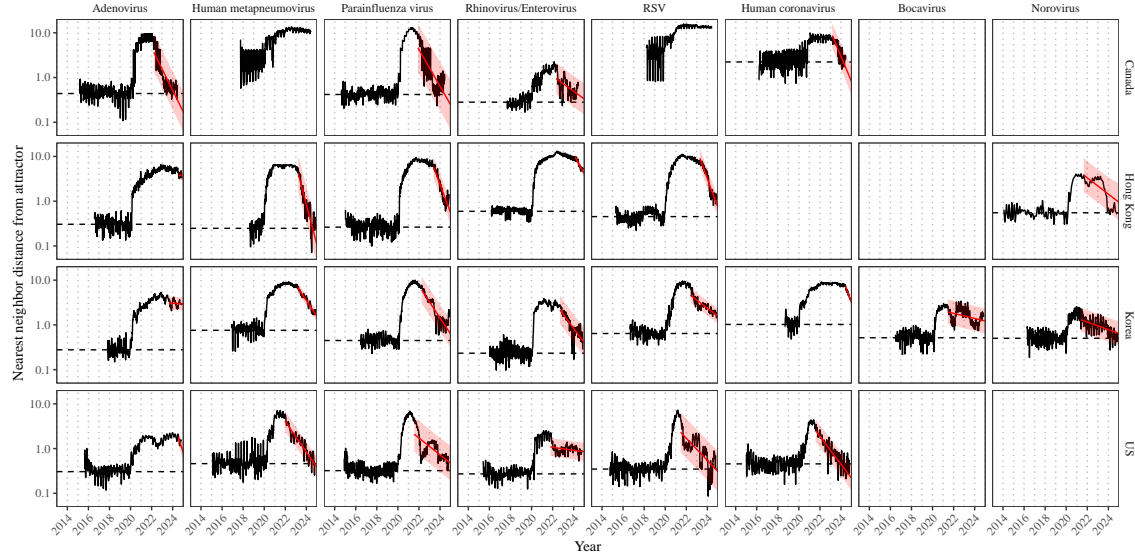


Figure S9: **Predicted timing of when each pathogen will return to their pre-pandemic cycles (zoomed out).** The dashed line in panel B indicates the end of 2024 (current observation time). Error bars represent 95% confidence intervals.



**Figure S10: Estimated time series of distance from attractor for each pathogen across Canada, Hong Kong, Korea, and the US using higher embedding dimensions.** Black lines represent the estimated distance from attractor. Red lines and shaded regions represent the linear regression fits and corresponding 95% confidence intervals. Dashed lines represent the average of the pre-pandemic nearest neighbor distances. A lower threshold is used for determining embedding dimensions with the false nearest neighbors approach, thereby yielding a higher embedding dimension.

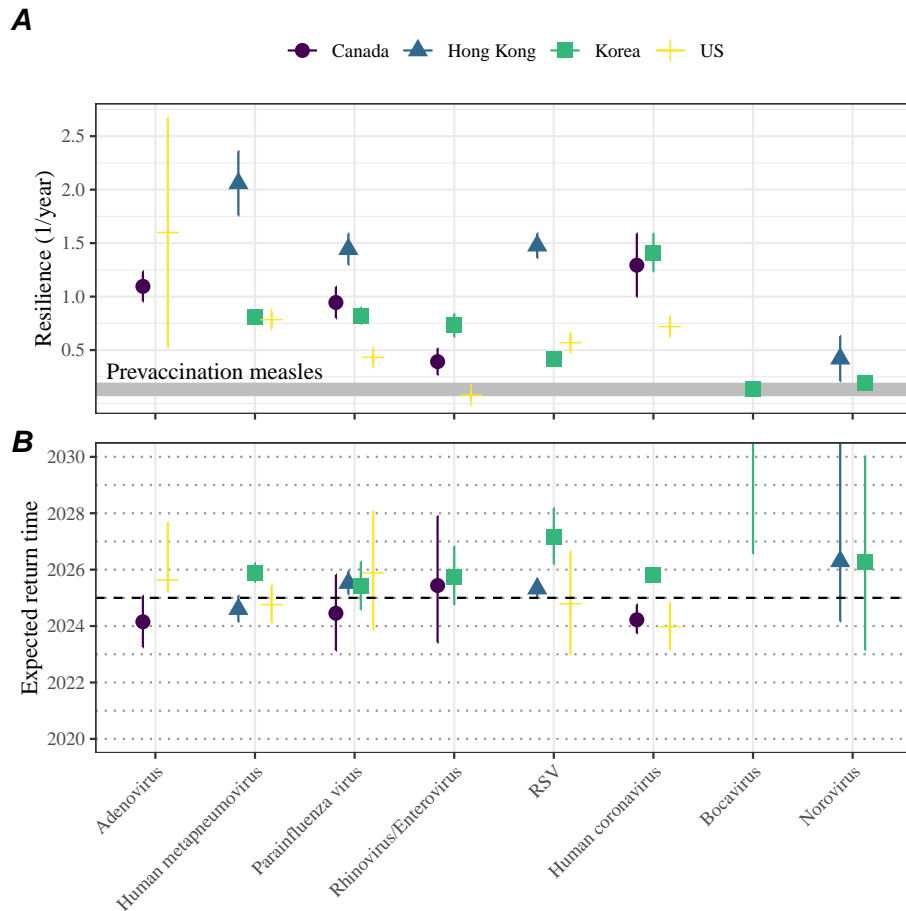


Figure S11: **Summary of resilience estimates using higher embedding dimensions.** (A) Estimated pathogen resilience. The gray horizontal line represents the intrinsic resilience of pre-vaccination measles dynamics. (B) Predicted timing of when each pathogen will return to their pre-pandemic cycles. The dashed line in panel B indicates the end of 2024 (current observation time). Error bars represent 95% confidence intervals. A lower threshold is used for determining embedding dimensions with the false nearest neighbors approach, thereby yielding a higher embedding dimension.

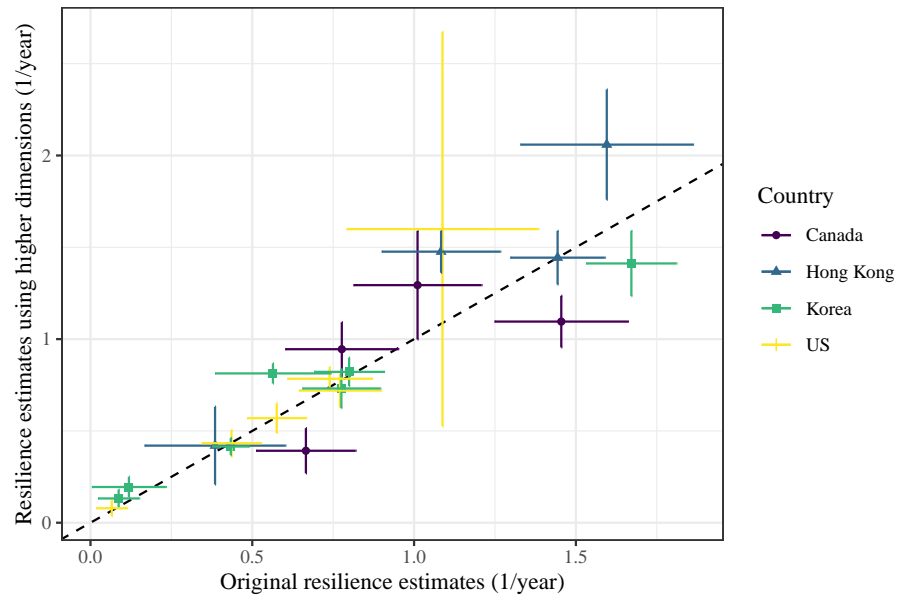


Figure S12: **Comparison of resilience estimates.** Each point represents a resilience estimate for a specific pathogen at a specific country. The x values represent the original resilience estimates presented in Figure 4. The y values represent the original resilience estimates presented in Supplementary Figure S11.

## 633 References

- 634 [1] Edward A Bender, Ted J Case, and Michael E Gilpin. Perturbation experiments  
635 in community ecology: theory and practice. *Ecology*, 65(1):1–13, 1984.
- 636 [2] Anthony R Ives and Stephen R Carpenter. Stability and diversity of ecosystems.  
637 *science*, 317(5834):58–62, 2007.
- 638 [3] Marten Scheffer, Jordi Bascompte, William A Brock, Victor Brovkin, Stephen R  
639 Carpenter, Vasilis Dakos, Hermann Held, Egbert H Van Nes, Max Rietkerk,  
640 and George Sugihara. Early-warning signals for critical transitions. *Nature*,  
641 461(7260):53–59, 2009.
- 642 [4] Stuart L Pimm. The structure of food webs. *Theoretical population biology*,  
643 16(2):144–158, 1979.
- 644 [5] Michael G Neubert and Hal Caswell. Alternatives to resilience for measuring  
645 the responses of ecological systems to perturbations. *Ecology*, 78(3):653–665,  
646 1997.
- 647 [6] Lance H Gunderson. Ecological resilience—in theory and application. *Annual  
648 review of ecology and systematics*, 31(1):425–439, 2000.
- 649 [7] Vasilis Dakos and Sonia Kéfi. Ecological resilience: what to measure and how.  
650 *Environmental Research Letters*, 17(4):043003, 2022.
- 651 [8] Jeanne C Chambers, Craig R Allen, and Samuel A Cushman. Operationalizing  
652 ecological resilience concepts for managing species and ecosystems at risk.  
653 *Frontiers in Ecology and Evolution*, 7:241, 2019.
- 654 [9] Rachel E Baker, Sang Woo Park, Wenchang Yang, Gabriel A Vecchi, C Jessica E  
655 Metcalf, and Bryan T Grenfell. The impact of COVID-19 nonpharmaceutical  
656 interventions on the future dynamics of endemic infections. *Proceedings of the  
657 National Academy of Sciences*, 117(48):30547–30553, 2020.
- 658 [10] Gabriela B Gomez, Cedric Mahé, and Sandra S Chaves. Uncertain effects of the  
659 pandemic on respiratory viruses. *Science*, 372(6546):1043–1044, 2021.
- 660 [11] Mihaly Koltai, Fabienne Krauer, David Hodgson, Edwin van Leeuwen, Marina  
661 Treskova-Schwarzbach, Mark Jit, and Stefan Flasche. Determinants of RSV  
662 epidemiology following suppression through pandemic contact restrictions. *Epi-  
663 demics*, 40:100614, 2022.
- 664 [12] Sang Woo Park, Brooklyn Noble, Emily Howerton, Bjarke F Nielsen, Sarah  
665 Lentz, Lilliam Ambroggio, Samuel Dominguez, Kevin Messacar, and Bryan T  
666 Grenfell. Predicting the impact of non-pharmaceutical interventions against  
667 COVID-19 on *Mycoplasma pneumoniae* in the United States. *Epidemics*,  
668 49:100808, 2024.

- 669 [13] Eric J Chow, Timothy M Uyeki, and Helen Y Chu. The effects of the COVID-19  
670 pandemic on community respiratory virus activity. *Nature Reviews Microbiology*,  
671 21(3):195–210, 2023.
- 672 [14] Georgiy V Bobashev, Stephen P Ellner, Douglas W Nychka, and Bryan T  
673 Grenfell. Reconstructing susceptible and recruitment dynamics from measles  
674 epidemic data. *Mathematical Population Studies*, 8(1):1–29, 2000.
- 675 [15] Bärbel F Finkenstädt and Bryan T Grenfell. Time series modelling of childhood  
676 diseases: a dynamical systems approach. *Journal of the Royal Statistical Society  
677 Series C: Applied Statistics*, 49(2):187–205, 2000.
- 678 [16] Floris Takens. Detecting strange attractors in turbulence. In *Dynamical Sys-  
679 tems and Turbulence, Warwick 1980: proceedings of a symposium held at the  
680 University of Warwick 1979/80*, pages 366–381. Springer, 2006.
- 681 [17] Alan Hastings, Karen C Abbott, Kim Cuddington, Tessa Francis, Gabriel Gell-  
682 ner, Ying-Cheng Lai, Andrew Morozov, Sergei Petrovskii, Katherine Scran-  
683 ton, and Mary Lou Zeeman. Transient phenomena in ecology. *Science*,  
684 361(6406):eaat6412, 2018.
- 685 [18] Matthew B Kennel, Reggie Brown, and Henry DI Abarbanel. Determining  
686 embedding dimension for phase-space reconstruction using a geometrical con-  
687 struction. *Physical review A*, 45(6):3403, 1992.
- 688 [19] Eugene Tan, Shannon Algar, Débora Corrêa, Michael Small, Thomas Stemler,  
689 and David Walker. Selecting embedding delays: An overview of embedding  
690 techniques and a new method using persistent homology. *Chaos: An Interdis-  
691 ciplinary Journal of Nonlinear Science*, 33(3), 2023.
- 692 [20] Samit Bhattacharyya, Per H Gesteland, Kent Korgenski, Ottar N Bjørnstad,  
693 and Frederick R Adler. Cross-immunity between strains explains the dynamical  
694 pattern of paramyxoviruses. *Proceedings of the National Academy of Sciences*,  
695 112(43):13396–13400, 2015.
- 696 [21] Bryan T Grenfell, Ottar N Bjørnstad, and Bärbel F Finkenstädt. Dynamics of  
697 measles epidemics: scaling noise, determinism, and predictability with the TSIR  
698 model. *Ecological monographs*, 72(2):185–202, 2002.
- 699 [22] Virginia E Pitzer, Cécile Viboud, Vladimir J Alonso, Tanya Wilcox, C Jessica  
700 Metcalf, Claudia A Steiner, Amber K Haynes, and Bryan T Grenfell. Environ-  
701 mental drivers of the spatiotemporal dynamics of respiratory syncytial virus in  
702 the United States. *PLoS pathogens*, 11(1):e1004591, 2015.
- 703 [23] Katharine R Dean, Fabienne Krauer, Lars Walløe, Ole Christian Lingjærde, Bar-  
704 bara Bramanti, Nils Chr Stenseth, and Boris V Schmid. Human ectoparasites

- 705 and the spread of plague in Europe during the Second Pandemic. *Proceedings*  
706 *of the National Academy of Sciences*, 115(6):1304–1309, 2018.
- 707 [24] Margarita Pons-Salort and Nicholas C Grassly. Serotype-specific immunity  
708 explains the incidence of diseases caused by human enteroviruses. *Science*,  
709 361(6404):800–803, 2018.
- 710 [25] Sarah Cobey and Edward B Baskerville. Limits to causal inference with state-  
711 space reconstruction for infectious disease. *PloS one*, 11(12):e0169050, 2016.
- 712 [26] Stephen M Kissler, Christine Tedijanto, Edward Goldstein, Yonatan H Grad,  
713 and Marc Lipsitch. Projecting the transmission dynamics of SARS-CoV-2  
714 through the postpandemic period. *Science*, 368(6493):860–868, 2020.
- 715 [27] Edward Goldstein, Sarah Cobey, Saki Takahashi, Joel C Miller, and Marc Lip-  
716 sitch. Predicting the epidemic sizes of influenza A/H1N1, A/H3N2, and B: a  
717 statistical method. *PLoS medicine*, 8(7):e1001051, 2011.
- 718 [28] Bob Carpenter, Andrew Gelman, Matthew D Hoffman, Daniel Lee, Ben  
719 Goodrich, Michael Betancourt, Marcus A Brubaker, Jiqiang Guo, Peter Li,  
720 and Allen Riddell. Stan: A probabilistic programming language. *Journal of*  
721 *statistical software*, 76, 2017.
- 722 [29] Stan Development Team. RStan: the R interface to Stan, 2024. R package  
723 version 2.32.6.